




Relativistic and spin-orbit dynamics at nonrelativistic intensities in strong-field ionizationAndrew S. Maxwell * and Lars Bojer Madsen *Department of Physics and Astronomy, Aarhus University, DK-8000 Aarhus C, Denmark* (Received 10 October 2023; revised 24 April 2024; accepted 13 August 2024; published 13 September 2024)

Spin-orbit dynamics and relativistic corrections to the kinetic energy in strong-field dynamics have long been ignored for near- and mid-infrared fields with intensities 10^{13} – 10^{14} W/cm², as the final photoelectron energies are considered too low for these effects to play a role. However, using a precise and flexible path-integral formalism, we include all correction terms from the fine-structure, Breit-Pauli Hamiltonian. This enables a treatment of spin, through coherent spin states, which is the first model to use this approach in strong-field physics. We are able to show that the most energetically rescattered wave packets are affected by relativistic kinetic energy corrections during rescattering. We probe these effects and show that they yield notable differences for a 1600-nm wavelength laser field on the dynamics and the photoelectron spectra. Furthermore, we find that the dynamical spin-orbit coupling is strongly overestimated if relativistic corrections to kinetic energy are not considered. Finally, we derive a new condition that demonstrates that relativistic effects begin to play a role at intensities many orders of magnitude lower than expected for the case of rescattering. Our findings may have important implications for imaging processes such as laser-induced electron diffraction, which includes high-energy photoelectron recollisions.

DOI: [10.1103/PhysRevA.110.033108](https://doi.org/10.1103/PhysRevA.110.033108)**I. INTRODUCTION**

Electron spin is a canonical example of the departure of the atomic scale world from our macroscopic one. The discovery of spin [1] carried huge fundamental significance, while also leading to a vast range of observable effects, from fine-structure splitting and the Zeeman [2] effect, to the Stern-Gerlach experiment and Mott scattering [3]. There are a huge range of applications exploiting spin, including spin-resonance imaging processes, atomic clocks, quantum sensors for magnetic fields, spin qubits, and spintronics (spin transport in solids) [3]. Despite its significance, until recently [4,5], the role of spin was ignored in strong-field processes driven by “nonrelativistic” laser intensities. The argument given is that at these intensities, the spin will not interact with the laser field, and that the energies reached in laser-driven recollisions (often taken to be $\approx 3.17U_p$ [6], U_p is the ponderomotive energy, i.e., the cycle-averaged kinetic energy of a free electron in the laser field) are insufficient for spin-orbit coupling or other relativistic effects to play a role.

Strong-field physics deals with the interaction of intense and short laser fields with matter. Through the control of a few recollision-based processes, this has enabled the measurement and manipulation of matter on the scale of attoseconds (10^{-18} s), giving birth to the field of attosecond physics [7–10] and attosecond laser pulses [11,12] via high-harmonic generation (HHG) [6,13]. One of the primary processes involved is above-threshold ionization (ATI) [14], which, in this context, is the strong-field (or tunnel) removal of an electron by the laser. After ionization, the continuum electron may

undergo laser-driven elastic scattering off the residual ion, sometimes referred to as high-order ATI (HATI) [15,16]. The processes of ATI and HATI have found use in imaging procedures, laser-induced electron diffraction (LIED) [17–21], and photoelectron holography [22–24]. In the former, the recolliding electron is used to provide diffraction images of its parent molecule. In photoelectron holography, the interference of electronic wave packets that recollide and those that do not is used to image the parent atom or molecule. In the case of LIED, long wavelengths, on the order of a few microns, are used to achieve high electronic recollision velocities. These hard recollisions closely probe the target, potentially leading to large spin-orbit coupling and large kinetic energies.

In the relativistic laser intensity regime ($I > 10^{16}$ W/cm²) (see, e.g., Refs. [25–34]), spin is often considered alongside other relativistic effects, note we have neglected works on high intensity and high frequency (in the so-called stabilization regime), as we are focused on fields with near-infrared and infrared frequencies. Popular ionization models such as the strong-field approximation (SFA) [35–37] were generalized to the relativistic regime [25,26], and many studies have considered spin-related effects (see, e.g., Refs. [28,31]). However, in order to estimate the intensity at which relativistic effects become relevant, it is common to employ classical Coulomb-free trajectories [27], which predicts that these effects should be negligible for intensities $I < 10^{16}$ W/cm². This is a good approach for the direct ATI electrons, but in the case of rescattered electrons, the Coulomb potential can allow for much higher kinetic energies to be reached. In this work, we will introduce a Coulomb adapted condition for backscattered trajectories. Some relativistic models have extended the relativistic SFA to account for the Coulomb potential (see,

*Contact author: andrew.maxwell@ucl.ac.uk

e.g., Refs. [33,34]) and derived cutoff limits for relativistic rescattering [32].

In the nonrelativistic regime, the effect of spin and spin-orbit coupling was found to play a role in atoms with appreciable internal spin-orbit coupling. Early work demonstrated spin-orbit effects in ion alignment with strong laser fields [38]. Spin-orbit effects in particular cases in single-photon [39] and multiphoton [40] ionization have long been known, but in Ref. [4], this was theoretically described for strong-field ionization with a circularly polarized laser field (later extended to include additional Coulomb effects [41]), where a general mechanism for producing spin-polarized electrons was developed. This mechanism depends on the preferential tunneling of “counter-rotating” electrons to the circular laser field [42–44]. The spin-polarized electrons were experimentally verified by Ref. [5], where Mott scattering was used to measure the spin polarization of the photoelectrons. Later experiments revealed different spin polarization across peaks in the photoelectron ATI spectra [45]. This effect has also been explored by a numerical solution of the Pauli equation [46], while some studies have solved the Dirac equation in the nonrelativistic regime [46–48]. Additional theoretical work has focused on effects due to Pauli symmetrization given initial singlet or triplet states [49,50], or the spin dynamics of the residual ion [51–56], related work using attosecond pulses has demonstrated the possibility to reveal time-resolved spin dynamics in the ion [57]. In a very recent work [58], inelastic recollision of the photoelectron with the ion was also considered, where tuning the evolution of the ionic spin could allow a spin flip, which has implications for recollision-based imaging process such as LIED.

Thus, the potential for spin and spin-orbit coupling to play a role in the photoelectron recollision processes has only just begun to be explored. In this work, we will explore the spin and spin-orbit coupling of the recolliding photoelectron in detail. In order to do this, we will extend the accurate and flexible path-integral approach, the Coulomb quantum-orbit strong-field approximation (CQSFA) [59–64]. This model has been developed in the spirit of the quantum-orbit formalisms of the SFA [65–67], that has enabled significant insight into ATI and recollision processes [15,16]. In its original formulation, the CQSFA was used extensively to understand holographic interference patterns that occur in photoelectron momentum distributions (PMDs) [68–71]. In these studies, a good qualitative agreement with numerical solutions of the time-dependent Schrödinger equation (TDSE) was possible for medium photoelectron energies of up to around $3-4U_p$. However, recent developments [72–74] have enabled exceptional quantitative agreement with the TDSE up to the highest rescattering energies of $10U_p$. These developments include the proper computation of the stability prefactor and Maslov phases [72], an improved algorithm for finding saddle-point solutions, the inclusion of a \sin^2 pulse envelope, and an improved method for computing the bound-state prefactors; all these improvements are combined in Ref. [74], and have been used in this work.

The CQSFA provides the ideal platform for understanding the spin-orbit effects of the recolliding photoelectron, providing an intuitive trajectory-based picture. In this work, we demonstrate the high level of agreement of the CQSFA for the

nonrelativistic spinless, few-cycle case, via comparison with a TDSE solver at a wavelength of 1600 nm for hydrogen at a typical intensity of 5×10^{13} W/cm². We demonstrate, even at this stage, that relativistic corrections are required to correctly describe the rescattered wave packet due to differences in the probability amplitude when including relativistic corrections. Thus, we present a derivation for the CQSFA that includes the Breit-Pauli relativistic corrections, in particular, a spin-orbit coupling term and corrections to the kinetic energy (or mass correction term). The inclusion of coherent-spin states allows for a dynamical description of spin with path integrals. We derive analytic expressions that describe the spin dynamics and evolution of the spin-orbit phase. We find that with the kinetic energy corrections, the rescattering dynamics is properly described, with trajectories no longer traveling faster than light. This leads to a noticeable change in the PMD probability that can be explained in terms of the trajectories. Furthermore, we consider the effect of initial spin alignment vs no spin alignment. If the relativistic kinetic energy corrections are not included, this leads to considerable differences that would be experimentally measurable. However, including the kinetic energy corrections leads to very modest differences for the two spin alignments. This demonstrates the importance of including the relativistic kinetic energy corrections when computing the effect of spin-orbit coupling. Finally, we derive analytical expressions to approximately identify the (back)scattering angles for which a relativistic treatment is required across a range of laser intensities.

The article is organized as follows. In Sec. II we briefly describe the theory for the nonrelativistic spinless CQSFA and TDSE solver. In Sec. III, we present the results of these models and investigate the rescattered trajectories. In Sec. IV, we present an alternative formulation of the CQSFA, including spin and other relativistic corrections. In Sec. V, analytical results are presented regarding the weak-coupling approximation and spin-orbit phase. In Sec. VI, we present the results with the newly derived theory, investigating the effect of the relativistic kinetic energy corrections and spin-orbit coupling terms. In Sec. VII, we derive limits to determine at which scattering angles a relativistic treatment is required. Finally, in Sec. VIII, we present our final conclusions. Atomic units are used throughout unless stated otherwise.

II. THEORY

A. CQSFA

We begin by giving a brief description of the CQSFA, which has been described in detail in its present accurate form in Ref. [74], while its initial development is described in Refs. [59,61,61,62].

We start from the nonrelativistic Hamiltonian for an atomic target in a strong field under the single-active-electron approximation, which may be written as

$$\hat{H}(t) = \hat{H}_0 + \hat{H}_I(t). \quad (1)$$

Here, \hat{H}_0 is the Hamiltonian atomic system, which, we write as $\hat{H}_0 = K(\hat{\mathbf{p}}) + U(\hat{\mathbf{r}})$, where $K(\hat{\mathbf{p}})$ and $U(\hat{\mathbf{r}})$ are general functions for the kinetic and potential energies, respectively, while $\hat{H}_I(t) = \hat{\mathbf{r}} \cdot \mathbf{E}(t)$ describes the interaction with the external laser field in the length gauge. We want to

compute the momentum-dependent transition amplitude $M(\mathbf{p}_f) = \langle \psi_{\mathbf{p}_f} | U(t, t_0) | \psi_0 \rangle$, where $|\psi_0\rangle$ is the initial bound state of the system, $|\psi_{\mathbf{p}_f}\rangle$ is a scattering state with asymptotic momentum \mathbf{p}_f , the final time $t \rightarrow \infty$, and the initial time $t_0 \rightarrow -\infty$. The transition amplitude may be written, still in an exact form [59,61], as

$$M(\mathbf{p}_f) = -i \int_{-\infty}^t dt' \langle \psi_{\mathbf{p}_f} | U(t, t') H_I(t') | \psi_0(t') \rangle. \quad (2)$$

Here, $U(t, t')$ is the time-evolution operator given by

$$U(t, t') = \hat{T} \exp \left(-i \int_{t'}^t d\tau \hat{H}(\tau) \right), \quad (3)$$

where \hat{T} exp denotes the time-ordered exponential. Including the resolution of the identity operator before $H_I(t')$ in Eq. (2), given by $\mathbb{1} = \int d^3 \mathbf{p}_0 |\tilde{\mathbf{p}}_0\rangle \langle \tilde{\mathbf{p}}_0|$, where $\tilde{\mathbf{p}}_0 = \mathbf{p}_0 + \mathbf{A}(t')$, yields

$$M(\mathbf{p}_f) = -i \lim_{t \rightarrow \infty} \int_{-\infty}^t dt \int d^3 \tilde{\mathbf{p}}_0 e^{iI_{\mathbf{p}_f}} d(\tilde{\mathbf{p}}_0, t') \times \langle \tilde{\mathbf{p}}_f | U(t, t') | \tilde{\mathbf{p}}_0 \rangle, \quad (4)$$

where $I_{\mathbf{p}}$ is the ionization potential of the bound state. The above equation allows for representation in path-integral form via time slicing [74,75],

$$\langle \tilde{\mathbf{p}}_f | U(t, t') | \tilde{\mathbf{p}}_0 \rangle = \prod_{n=1}^N \left[\int d^3 \tilde{\mathbf{p}}_n \right] \prod_{n=1}^{N+1} \left[\int \frac{d^3 \mathbf{r}_n}{(2\pi)^3} \right] e^{i\mathcal{A}_N},$$

where

$$\mathcal{A}_N = - \sum_{n=1}^{N+1} [\mathbf{r}_n \cdot (\tilde{\mathbf{p}}_n - \tilde{\mathbf{p}}_{n-1}) + \Delta t H(\tilde{\mathbf{p}}_n, \mathbf{r}_n, t_n)]. \quad (5)$$

The limit $N \rightarrow \infty$ is now taken in order to turn the product of integrals into path integrals,

$$M(\mathbf{p}_f) = -i \int_{-\infty}^{\infty} dt' \int_{\mathbf{r}(t')} \frac{\mathcal{D}' \mathbf{r}}{(2\pi)^3} \int^{\mathbf{p}(t')} \mathcal{D}' \mathbf{p} e^{iS[\mathbf{r}, \mathbf{p}, t']} d(\tilde{\mathbf{p}}_0, t'), \quad (6)$$

with $d(\tilde{\mathbf{p}}_0, t') = \langle \mathbf{p}_0 + \mathbf{A}(t') | H_I(t') | \psi_0 \rangle$,

$$S[\mathbf{r}, \mathbf{p}, t'] = I_{\mathbf{p}} t' - \mathbf{p}(t') \cdot \mathbf{r}(t') - \int_{t'}^{\infty} d\tau (\tilde{\mathbf{p}} \cdot \mathbf{r} + H[\mathbf{r}, \mathbf{p}, t']), \quad (7)$$

and $H[\mathbf{r}, \mathbf{p}, t']$ is the classical Hamiltonian.¹ The action in Eq. (7) results from enforcing an initial condition in position space and a final limit in momentum space, giving rise to the boundary term $\mathbf{p}(t') \cdot \mathbf{r}(t')$, i.e., we are in the mixed representation. These restrictions are denoted by the primes on \mathcal{D}' 's (full details are given in Ref. [74]). For atoms, the initial position is the origin, hence, $\mathbf{r}(t') = \mathbf{0}$, and $\mathbf{p}(t') \cdot \mathbf{r}(t')$ may be dropped. Note, we define $\mathbf{p}_0 = \mathbf{p}(t') = \mathbf{p}(\text{Re}[t'])$, which

¹Technically, $H[\mathbf{r}, \mathbf{p}, t']$ is the Weyl transformed quantum-mechanical Hamiltonian [115], which differs from the classical Hamiltonian $H[\mathbf{p}, \mathbf{r}, t'] = K[\mathbf{p}] + U[\mathbf{r}] + H_I(t')$ by orders of \hbar^2 ; however, these differences may be discarded given we will be applying the saddle-point approximation that already neglects the quadratic power of \hbar .

results from taking momentum fixed during tunneling (this approximation is explained in more detail in Appendix A).

The transition amplitude of Eq. (6) is then evaluated via the saddle-point approximation

$$M(\mathbf{p}) = -i \sum_s \sqrt{\frac{2\pi i}{\partial^2 S / \partial t'^2}} \frac{e^{-i\pi\nu/2}}{\sqrt{|J|}} d(\tilde{\mathbf{p}}_{0s}, t_s) e^{iS[\mathbf{r}_s, \mathbf{p}_s, t_s]}, \quad (8)$$

where $\underline{J} = \frac{\partial \mathbf{p}_f}{\partial \mathbf{p}_0}$, $J = \det(\underline{J})$, and ν is the Maslov index, which may be determined by computing \underline{J} at all points in time and counting the number of focal points ($J = 0$) [72,74]. The sum runs over all solutions to the saddle-point equations, which are given by

$$(\mathbf{p}_{0s} + \mathbf{A}(t_s))^2 + 2I_{\mathbf{p}} = 0, \quad (9)$$

$$\dot{\mathbf{r}}_s(t) = \nabla_{\mathbf{p}} K[\mathbf{p}_s + \mathbf{A}(t_s)] \quad \text{and} \quad \dot{\mathbf{p}}_s(t) = -\nabla_{\mathbf{r}} U[\mathbf{r}_s]. \quad (10)$$

Equation (9) leads to complex ionization times t_s meaning the integral in Eq. (7) is done in two parts, first over imaginary time from t_s to $\text{Re}[t_s]$ associated with tunneling, then over real time from $\text{Re}[t_s]$ to ∞ , associated with real-space continuum propagation (see Appendix A for more details).

The CQSFA solves a boundary value problem known as the inverse problem, i.e., all solutions of Eqs. (9) and (10) (i.e., trajectories or quantum orbits) are found satisfying $\mathbf{r}(t') = \mathbf{0}$ and $\mathbf{p}(t \rightarrow \infty) = \mathbf{p}_f$. There will be multiple solutions for each final momentum point; each solution can be uniquely determined by its initial momentum coordinate \mathbf{p}_0 . Thus, the inverse problem reduces to finding the set of initial momentum coordinates \mathbf{p}_0 , for each final momentum \mathbf{p}_f .

The approach just described is different from the majority of models, which use a forward approach and bin trajectories with similar final momenta, which requires small bins and many trajectories to resolve interferences, while the inverse approach allows for many fewer trajectories. Furthermore, recent work [76] has identified that forward approaches do not yield the correct sampling weight in terms of the Jacobian J , leading to $1/|J|$ instead of the correct $1/\sqrt{|J|}$ computed by inverse approaches. The downside of the inverse approach is that it is much harder to solve, and approaches can be less general. In previous works [61–63], solutions were found by “exploring” the manifold of solutions, i.e., changing parameters to find “connected” solutions. This method is very fast but has two disadvantages: (i) it requires preknowledge of the shape of the manifold and, where solutions lie, which changes from system to system; (ii) it assumes all solutions can be reached in this way, which is not the case. In this work, we used an alternative method [74] where the solutions are found by initial random sampling of \mathbf{p}_0 , and adaptively concentrating guesses in \mathbf{p}_0 regions where dense clusters of solutions are found. This method is more general and allows all solutions to be found regardless of the system.

The distinct solutions for each \mathbf{p}_f do not have an exhaustive classification, however, in the case of linearly polarized fields, four broad types of orbit can be defined that can helpfully classify behavior. This classification uses the tunnel exit

$$z_0 = \text{Re} \left(\int_{t_s}^{\text{Re}[t_s]} d\tau A_z(\tau) \right), \quad (11)$$

TABLE I. Orbit classification used in the CQSFA for monochromatic linearly polarized fields. The labeling 1 to 4 classifies the orbit with two different conditions, the signs of $\Pi_z = z_0 p_{fz}$ and $\Pi_\perp = p_{fx} p_{0x} + p_{fy} p_{0y}$, respectively. The behavior in the fourth column indicates the expected dynamics of the specific types of orbits.

Orbit	Π_z	Π_\perp	Behavior
1	+	+	Direct
2	-	+	Laser-driven deflection
3	-	-	Forward scattered
4	+	-	Rescattered

and initial momentum perpendicular to the laser polarization $\mathbf{p}_{0\perp}$, and compares their sign with p_{fz} and $\mathbf{p}_{f\perp}$, respectively. Then we may define $\Pi_z = z_0 p_{fz}$ and $\Pi_\perp = p_{fx} p_{0x} + p_{fy} p_{0y}$. This is the same definition as in Ref. [74], which generalizes the commonly employed two-dimensional (2D) classification [61,73,77] to three dimensional (3D). The classification, summarized in Table I, is as follows: $\Pi_z > 0 \wedge \Pi_\perp > 0$: orbit 1, associated with direct trajectories that do not return to the parent atom; $\Pi_z < 0 \wedge \Pi_\perp > 0$: orbit 2, describes trajectories that undergo a laser-driven return but do not interact strongly with the parent atom; $\Pi_z < 0 \wedge \Pi_\perp < 0$: orbit 3, trajectories that forward scatter off the parent atom; and $\Pi_z < 0 \wedge \Pi_\perp < 0$: orbit 4, associated with trajectories that backscatter off parent atom. Note that there may be more than one valid solution of each type.

Examples typifying the classifications are given in Fig. 1(a); laser parameters are given in the caption. Here, we see typical examples of orbits 1–4, as well as an “atypical” orbit 4 (labeled 4b), along with the corresponding ionization times in the panel below. For this study, we are most interested in the rescattered trajectories of orbit 4. The tunnel exit of the “typical” orbit 4 lies at $z_0 \approx -15$ a.u.; from here the laser drives the trajectory away and then back again, undergoing a laser-driven return, as shown in Fig. 1(a). Thus, this solution belongs to a well-studied category of returning trajectory known from HHG and ATI [13,15]. These orbits come in pairs, long and short. Here, we have only plotted the long trajectory, as the short’s path would be very similar. These pairs can be seen in Fig. 1(b) in every half-cycle by the black loops extending in opposite directions each half-cycle (located at ~ 2.1 cycles for negative p_{fz} and ~ 2.5 cycles for positive p_{fz}), where a black square marks the long orbit 4 solution of interest. The solution pairs form loops because at a classical boundary, they coalesce, forming the rescattering ridge in the PMD (see Fig. 2). In contrast, the directly recolliding orbit 4b has a tunnel exit of $z_0 \approx -20$ a.u. close to orbit 1’s tunnel exit. Instead of undergoing a laser-driven recollision, the initial conditions are such that the trajectory returns before the laser has considerably changed sign. These trajectories also occur every half-cycle and are connected to the “typical” recolliding orbits via orbit 3 (in red) on a continuous manifold. Orbit 4b ionizes far from the peak at near zero field, thus the probability of these orbits is very low, however, they undergo a very strong recollision, so provide an interesting case to study. If the probability of these trajectories could be increased, they could be used for probing targets very strongly.

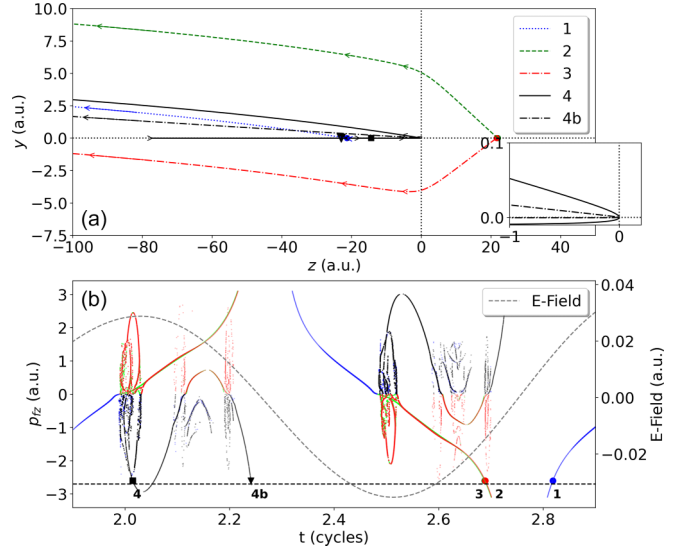


FIG. 1. Example trajectories for all 4 orbits (a), and the times of ionization for different final momenta p_{fz} (b). In the case of orbit 4, two solutions are shown, one “regular” laser-driven recollision, and one “directly” recolliding, labeled 4b. The laser is linearly polarized along the z axis. The tunnel exits are marked by circles for orbits 2 and 3, a square for 4 and a triangle for 4b. (a) Shows the four orbit types, the y axis has been stretched to better show the detail. (b) Plots the real time of ionization vs the p_{fz} momentum over a single laser cycle, with the six-cycle electric field superimposed. The ionization target is hydrogen, the laser wavelength is $\lambda = 1600$ nm, and the intensity is $I_0 = 5 \times 10^{13}$ W/cm². An inset showing the dynamics of orbits 4 and 4b close to the core is given, with its region marked by the rectangle (a). The final perpendicular momentum is chosen to be $p_{fx} = 0.0$ a.u., $p_{fy} = 0.05$ a.u., while in (a) $p_{fz} = -2.704$ a.u., which is denoted by the black dashed horizontal line in (b). Note the ionization times for orbit 2 in (b) are almost the same as those for orbit 3, and thus mostly obscured. The solutions corresponding to the trajectories plotted in (a) are marked on (b) by circles for orbits 2 and 3, a square for 4 and a triangle for 4b on the dashed line.

B. TDSE

To benchmark the CQSFA results, we solve the TDSE using the freely available QPROP [78] software. QPROP is a single-active-electron TDSE solver, which implements a fast and accurate method for the calculation of PMD using the i-SURFF projection method. To model hydrogen, a Coulomb potential is employed. In this computation, we considered angular momenta up to $l = 200$, grid spacing $\Delta r = 0.1$ a.u., and time step $\Delta t = 0.05$ a.u., and we checked the results for convergence.

In both the CQSFA and QPROP we consider a \sin^2 laser field, where the vector potential is defined by

$$\mathbf{A}(t) = 2\sqrt{U_p} \sin^2\left(\frac{\omega t}{2N}\right) \cos(\omega t + \phi) \hat{\mathbf{z}}, \quad (12)$$

with N being the number of laser cycles of the vector potential envelope, while U_p is the ponderomotive energy or quiver energy of the free electron in the laser field, which is proportional to the peak laser intensity $I_0 = 2U_p c \epsilon_0 \omega^2$. The angular frequency is given by ω and the carrier envelope phase (CEP)

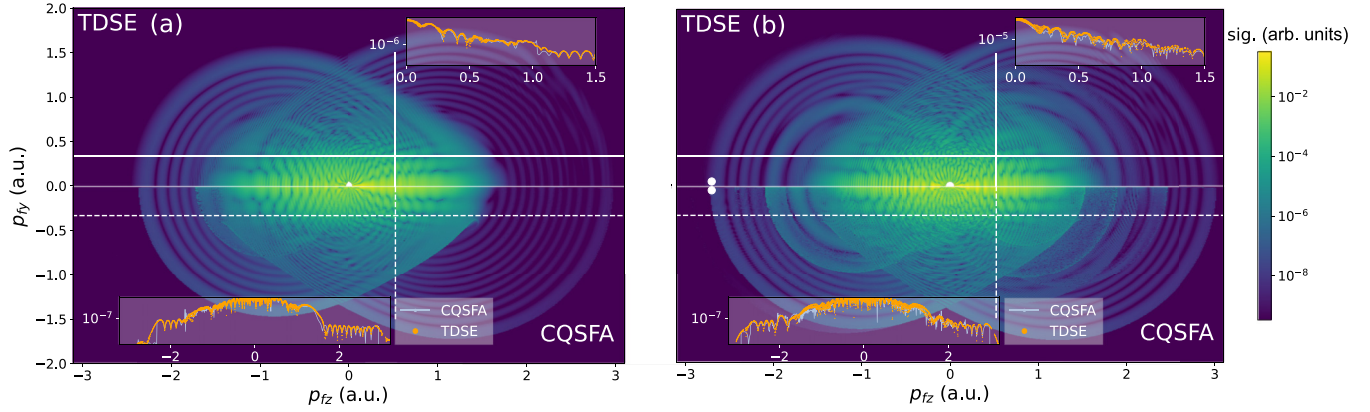


FIG. 2. Comparison of photoelectron momentum distributions (PMDs) for strong-field ionization of hydrogen computed using the TDSE and CQSFA, for a four-cycle and six-cycle \sin^2 pulse, [(a) and (b), respectively]. The upper half of each panel is computed using the TDSE solver QPROP, while the lower half is computed using the CQSFA. The insets show line-out plots of the TDSE and CQSFA PMDs. With the horizontal lines showing the region plotted in the bottom insets, and the vertical lines showing the region plotted in the top insets. The intensity is $I_0 = 5 \times 10^{13}$ W/cm² and wavelength $\lambda = 1600$ nm, the target is hydrogen with $I_p = 0.5$ a.u. The dots to the left in (b) correspond to final momenta of the example trajectories plotted in Figs. 1 and 3.

is given by ϕ . We focus on a wavelength $\lambda = 1600$ nm, i.e., $\omega = 0.0285$ a.u.

III. NONRELATIVISTIC RESULTS

In Fig. 2, we show a validation of the CQSFA vs the nonrelativistic TDSE with PMDs for hydrogen at a wavelength of 1600 nm for a four-cycle and six-cycle \sin^2 pulse [Figs. 2(a) and 2(b), respectively]. Very good agreement is seen between the two models across the whole momentum region. There is some deviation across classical boundaries at higher energies, seen in the line-out insets, where there is a more abrupt change from higher signal to lower signal as the classical boundary is crossed. Improved agreement here can only be achieved by accounting for correctly treating the coalescing long and short orbit 4 solutions, seen in Fig. 1, in a manner similar to the uniform approximation [79] applied to the equivalent SFA orbit (see, e.g., [80]).

The high-energy rings visible in Fig. 2(a) [around $(p_{fz}, p_{fy}) = (-2.0, 0.0)$] and Fig. 2(b) [around $(p_{fz}, p_{fy}) = (-2.5, 0.0)$] are particularly well captured. Previously, these have not been very well described by the CQSFA, but now additional orbit 4 contributions have been included that lead to very good agreement. The high-energy rings can be completely attributed to typical pairs of orbit 4, where the interference between long and short pairs gives the ringlike interference, previously only the long orbit was included in the CQSFA. In Fig. 2(b), the leftmost high-energy rings [around $(p_{fz}, p_{fy}) = (-2.5, 0.0)$] can be attributed to the orbit 4 pairs ionized near the peak at 2 cycles [Fig. 1(b)], while the rightmost high-energy rings [around $(p_{fz}, p_{fy}) = (3.0, 0.0)$] can be attributed to the orbit 4 pairs ionized near the peak at 2.5 cycles [see Fig. 1(b)].

The general high level of agreement seen in Fig. 2 validates the CQSFA approach, allowing the use of the trajectory-based machinery for interpretation and to probe the physics in detail. This also provides an easy platform to extend the formalism to include additional effects,

such as the spin-orbit coupling during photoelectron recollisions.

In Fig. 3, we plot metrics for five example high-energy rescattered trajectories following ionization of hydrogen for the six-cycle laser pulse, in preparation for including spin-orbit coupling dynamics; this includes the evolution of the velocity [Fig. 3(a)], distance from the origin [Fig. 3(b)], and the kinetic energy, potential, and spin-orbit phase terms in the action [Fig. 3(c)]. Here, Figs. 3(a)–3(c) correspond to the nonrelativistic CQSFA, while Figs. 3(d)–3(f) correspond to the CQSFA with relativistic corrections. We choose two pairs of rescattered trajectories that are ionized near the field peaks at 2 [labeled 4L2 and 4S2] and 3 [labeled 4L3 and 4S3] laser cycles [see ionization times marked on the laser field in Fig. 3(a)] and recollide around field crossings after $\frac{2}{3}$ to $\frac{3}{4}$ of a cycle of propagation; note this differs from the well-known $\frac{2}{3}$ result [15] due to the inclusion of the Coulomb field. These trajectories are the previously discussed orbit 4 long [4L] and short [4S] pairs, responsible for the high-energy ringlike structures in Fig. 2. We also include orbit 4b in Fig. 3. As previously mentioned orbit 4b has a low probability, so no clear features are visible in the spectrum in Fig. 2, however, it undergoes a very high-energy recollision, so is a useful test case.

Despite employing nonrelativistic intensities and all final photoelectron speeds being far from relativistic, the momentum transfer during recollision is very high. This can be seen in Fig. 3(a) by the large superluminal velocity spikes, occurring during recollisions. The long and short orbit 4 trajectories consistently reach $v \approx 2c$, while for the directly recolliding orbit $v \approx 6c$. These fast speeds are due to how strongly the core is probed; Fig. 3(b) shows that the trajectory's distance from the origin goes below 10^{-5} a.u. Note, that the trajectories and their velocity are *not* observable, and so care must be taken in interpreting these dynamics. However, we note that for a sizable part of the recolliding wave packet, these fast velocities are reached, which motivates study of the effect of relativistic effects on

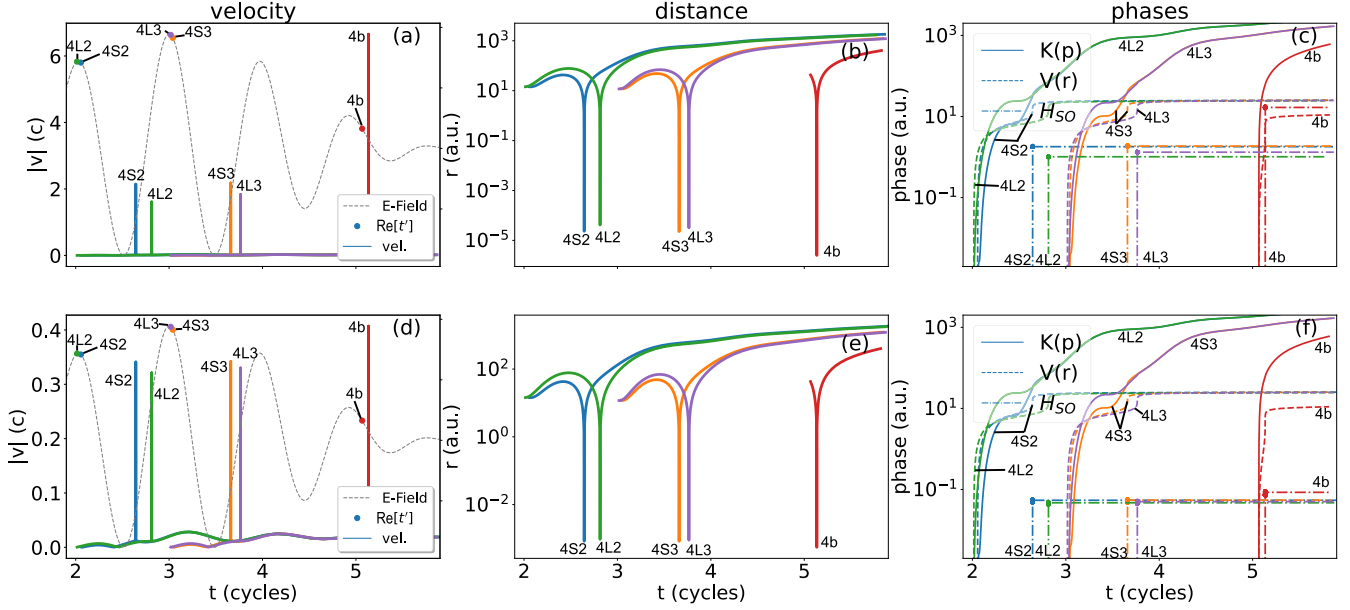


FIG. 3. Examples of velocity transfer and resulting phases picked up by rescattered orbit 4 trajectories, following strong-field ionization of hydrogen. Note that (a)–(c) correspond to the nonrelativistic CQSFA, while (d)–(f) correspond to the CQSFA with relativistic corrections. All lines are labeled with the solutions type: “4LC” and “4SC” are used for the long and short solutions, respectively, where “C” is the number of laser cycles that the ionization times occur at, being 2 or 3 for the solutions shown. The label “4b” denotes the 4b solution that is ionized near the fifth laser cycle. Consistent colors are used for each solution. (a), (d) Velocity over time given by colored lines (with abrupt spikes at recollisions) with the laser field plotted by a dashed line, where ionization times are marked on the field by colored circles, where the color of the circle and velocity line corresponds to particular orbits. (b), (e) Distance over time given by colored lines, where the colors match the same orbits as (a). (c), (f) The phase acquired from kinetic energy $K(p)$ (solid lines), potential energy $V(r)$ (dashed lines), and spin-orbit coupling H_{SO} [see Eqs. (50) and (51)] (dotted-dashed lines with an abrupt increase during recollision), which is given by the time integral of these quantities over each trajectory. The approximation to the spin-orbit phase, given by Eq. (54), is plotted in (c) and (f) as colored circles, as before the colors match the orbits in (a). The final momentum of all trajectories is the same as Fig. 1 $\mathbf{p}_f = (0.0, 0.05, -2.704)$; this point is indicated on Fig. 2.

the rescattered PMD. However, these high speeds are only reached for very short time periods, within a single attosecond. Thus, if it is for such short times, can it be simply neglected?

The phases in Fig. 3(c), where we plot the time integral of the kinetic energy $K(t)$, potential energy $V(t)$, and spin-orbit interaction $H_{SO}(t)$ [see Eq. (15)], help us to understand the importance of these very fast speeds over very short time periods. Given that the atomic core is probed so strongly, a large phase due to spin-orbit coupling is acquired. In the case of the directly recolliding trajectory, the spin-orbit phase (dotted-dashed red line labeled 4b) actually exceeds the phase picked up from the Coulomb potential (dashed red line labeled 4b). This is unexpected and requires careful analysis. It seems likely that these results may be overestimated while they include these fast trajectories. Crucially, the spin-orbit phase only really appreciably changes in the attosecond time period when superluminal velocities are reached. This can be seen from the highly abrupt change in the dashed-dotted lines in Fig. 3(c).

Overall, in Fig. 2, there is very good agreement with the TDSE, which suggests that the CQSFA methodology is correct despite the unphysical trajectories. One way to address this dichotomy is to include relativistic corrections that will lead to relativistic equations of motion for the trajectories, thus preventing superluminal velocities.

IV. FORMULATION OF RELATIVISTIC CQSFA

The results in Fig. 3 show that the trajectories in the CQSFA corresponding to the rescattered part of the wave packet gain unexpected large velocities, which warrants a relativistic treatment including spin-orbit coupling. The starting point for this is the Dirac equation, but as we are not considering relativistic laser intensities we will consider the expansion of the Dirac equations, up to terms of order $(v/c)^2$ [81]. The laser field may be included through minimal coupling: this gives what is sometimes referred to as the Breit-Pauli Hamiltonian

$$\hat{H}(t) = \frac{1}{2}[\hat{\mathbf{p}} + \mathbf{A}(\hat{\eta})]^2 + \hat{\mathbf{S}} \cdot \mathbf{B}(\hat{\eta}) - \frac{1}{8c^2}[\hat{\mathbf{p}} + \mathbf{A}(\hat{\eta})]^4 + V(\hat{\mathbf{r}}) - \frac{1}{8c^2}\nabla_{\mathbf{r}}^2 V(\hat{\mathbf{r}}) + \frac{\partial V(|\hat{\mathbf{r}}|)}{2c^2|\hat{\mathbf{r}}|}\hat{\mathbf{L}} \cdot \hat{\mathbf{S}}, \quad (13)$$

where $\hat{\eta} = \omega t - \mathbf{k} \cdot \hat{\mathbf{r}}$, $\mathbf{A}(\hat{\eta})$ and $\mathbf{B}(\hat{\eta})$ are the magnetic vector potential and magnetic field, respectively, while $\hat{\mathbf{L}} = \hat{\mathbf{r}} \times [\hat{\mathbf{p}} + \mathbf{A}(\hat{\eta})]$ is the angular momenta, $\hat{\mathbf{S}} = \hat{\sigma}/2$ is the spin operator, and $\hat{\sigma} = \sigma_x \hat{x} + \sigma_y \hat{y} + \sigma_z \hat{z}$ is the Pauli vector, constructed from the Pauli matrices.

Given that the wavelength of the laser field is not too long (or too short) [82] we may apply the dipole approximation,

which allows the velocity and length gauge forms of the Hamiltonian

$$\hat{H}_v(t) = K(\hat{\mathbf{p}}) + U(\hat{\mathbf{r}}) + \mathbf{C}_{\text{SO}}(\hat{\mathbf{r}}, \hat{\mathbf{p}}) \cdot \hat{\mathbf{S}}, \quad (14)$$

$$\hat{H}_l(t) = \underbrace{K(\hat{\mathbf{p}}) + U(\hat{\mathbf{r}})}_{\hat{H}_0} + \underbrace{\mathbf{C}_{\text{SO}}(\hat{\mathbf{r}}, \hat{\mathbf{p}}) \cdot \hat{\mathbf{S}}}_{\hat{H}_{\text{SO}}} + \hat{H}_I(t) \quad (15)$$

with

$$K(\hat{\mathbf{p}}) = K_0(\hat{\mathbf{p}}) + K_1(\hat{\mathbf{p}}) = \frac{\hat{\mathbf{p}}^2}{2} - \frac{\hat{\mathbf{p}}^4}{8c^2}, \quad (16)$$

$$U(\hat{\mathbf{r}}) = U_0(\hat{\mathbf{r}}) + U_1(\hat{\mathbf{r}}) = V(\hat{\mathbf{r}}) - \frac{\nabla_{\mathbf{r}}^2 V(\hat{\mathbf{r}})}{8c^2}, \quad (17)$$

$$\mathbf{C}_{\text{SO}}(\hat{\mathbf{r}}, \hat{\mathbf{p}}) = \frac{\partial}{\partial r} V(|\hat{\mathbf{r}}|) \hat{\mathbf{r}} \times \hat{\mathbf{p}}, \quad (18)$$

and $\hat{H}_I(t) = \mathbf{E}(t) \cdot \hat{\mathbf{r}}$ and $\hat{\mathbf{p}} = \hat{\mathbf{p}} + \mathbf{A}(t)$. The relativistic correction terms to the kinetic and potential energies (the Dyson correction), $K_1(\hat{\mathbf{p}})$ and $U_1(\hat{\mathbf{r}})$, still permit the solution given in Eq. (8), as here we assumed general forms for the kinetic and potential energies. The spin and spin-orbit coupling can, however, not be treated through the same path-integral approach that we used before, as we must consider the additional spin degree of freedom and coupling between them. In fact, historically a proper treatment of spin by path integrals took some time to develop.

In order to describe spin in a path-integral framework, we require a mapping of the spin to a continuous variable. The treatment of spin in terms of so-called coherent spin states [an irreducible representation for $\text{SU}(2)$] [83,84] does just this. In its most general form an $\text{SU}(2)$ coherent spin state can be written as

$$|z; S\rangle = \frac{e^{zS_+} |S, m_s = -S\rangle}{(1 + |z|^2)^S}. \quad (19)$$

For a spin- $\frac{1}{2}$ ($S = \frac{1}{2}$) system, dropping all the S 's, this may be written as

$$|z\rangle = \frac{|\downarrow\rangle + z|\uparrow\rangle}{\sqrt{1 + |z|^2}}, \quad (20)$$

where we use $|\uparrow\rangle$ ($|\downarrow\rangle$) to denote $m_s = \frac{1}{2}$ ($m_s = -\frac{1}{2}$). These states map spin states to the complex plane (see Fig. 4). Some key values are $|z \rightarrow 0\rangle = |\downarrow\rangle$, $|z \rightarrow \infty\rangle = |\uparrow\rangle$, $|z \rightarrow 1\rangle = |+\rangle$ and $|z \rightarrow -1\rangle = |-\rangle$.

A vital step when deriving a path-integral representation of a propagator is insertion of the resolution of the identity in time-sliced amplitudes. For coherent spin states the resolution of the identity may be written as

$$I_S = \int d\mu_S(z) |z; S\rangle \langle z; S|, \quad d\mu_S(z) = \frac{2S+1}{\pi} \frac{d^2Z}{(1 + |z|^2)^2}. \quad (21)$$

It is useful to apply this formalism to building eigenstates of the field-free system, i.e., $\hat{H}_{0,\text{SO}} = \hat{H}_0 + \hat{H}_{\text{SO}}$. Consider an initial state with quantum numbers j and m_j , built using the standard angular momentum addition rules e.g., see Ref. [4])

$$|\Phi_{jm_j}\rangle = \sum_{m, m_s} \langle l, S, m, m_s | l, S, j, m_j \rangle \otimes |\psi_{lm}\rangle |S; m_s\rangle, \quad (22)$$

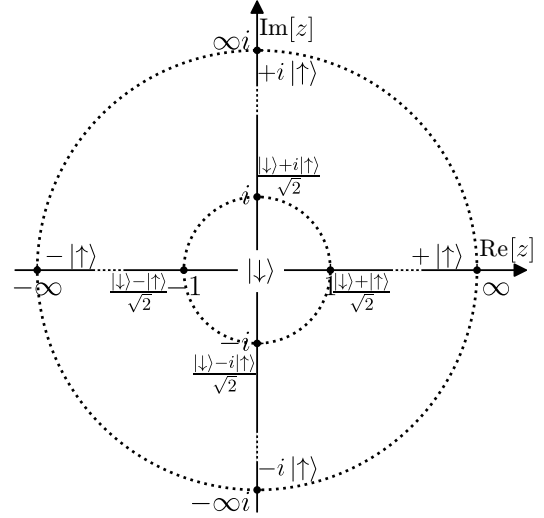


FIG. 4. The mapping of the complex plane to coherent spin states $|z\rangle$, given by Eq. (20). Some key values are marked by black filled circles and their corresponding states are given by adjacent labels.

where $|\psi_{l,m}\rangle$ is an eigenstate of the square of the orbital angular momentum and its projection on the quantization axis \hat{L}_z . For $S = \frac{1}{2}$ we can write $|\Phi_{jm_j}\rangle$ in terms of the coherent spin state

$$|\Phi_{jm_j}\rangle = \sum_m f_{lm}^{jm_j} |z_{lm}^{jm_j}\rangle \otimes |\psi_{lm}\rangle \quad (23)$$

with $f_{lm}^{jm_j} = C_{lm, \frac{1}{2} - \frac{1}{2}}^{jm_j} \sqrt{1 + |z_{lm}^{jm_j}|^2}$, $z_{lm}^{jm_j} = C_{lm, \frac{1}{2} \frac{1}{2}}^{jm_j} / C_{lm, \frac{1}{2} - \frac{1}{2}}^{jm_j}$, and $C_{lm, S m_s}^{j m_j} = \langle l, S, m, m_s | l, S, j, m_j \rangle$ are Clebsch-Gordan coefficients. Thus, the initial spin state is represented through a sum of coherent spin states. Thus, allowing an initial-fine-structure state ($|\Phi_{jm_j}\rangle$) [85], with quantum numbers j , and m_j , and energy E_{jm_j} written in terms of coherent spin states.

The transition amplitude can be defined for ionization starting in the bound state $|\Phi_{jm_j}\rangle$, and finishing in a continuum spin state $|\psi_{\mathbf{p}}, z\rangle = |\psi_{\mathbf{p}}\rangle \otimes |z\rangle$, at $t \rightarrow \infty$. The amplitude is then given by

$$\begin{aligned} M(\mathbf{p}_f, z) &= \langle \psi_{\mathbf{p}_f}, z | U(t, t_0) | \Phi_{jm_j} \rangle \\ &= -i \int_{-\infty}^t dt' \langle \psi_{\mathbf{p}}, z | U(t, t') H_I(t') | \Phi_{jm_j} \rangle e^{-iE_{jm_j}t'}. \end{aligned} \quad (24)$$

As before, we insert the resolution of the identity $\mathbb{1}_3 = \int d^3\tilde{\mathbf{p}}_0 |\tilde{\mathbf{p}}_0\rangle \langle \tilde{\mathbf{p}}_0|$, where $\tilde{\mathbf{p}}_0 = \mathbf{p}_0 + \mathbf{A}(t')$:

$$\begin{aligned} M(\mathbf{p}_f, z_f) &= -i \int_{t_0}^t dt' \int d^3\tilde{\mathbf{p}}_0 \langle \psi_{\mathbf{p}}, z_f | U(t, t') | \tilde{\mathbf{p}}_0 \rangle \\ &\quad \times \langle \tilde{\mathbf{p}}_0 | \hat{H}_I(t') | \Phi_{jm_j} \rangle e^{-iE_{jm_j}t'}. \end{aligned} \quad (25)$$

To proceed, we must expand the spin state, so we can exploit the fact that $[\hat{H}_I(t), \hat{\mathbf{S}}] = 0$,

$$\langle \tilde{\mathbf{p}}_0 | \hat{H}_I(t') | \Phi_{jm_j} \rangle = \sum_m |z_{lm}^{jm_j}\rangle d_m(\tilde{\mathbf{p}}_0, t') \quad (26)$$

with $d_m(\mathbf{p}_0, t') = f_{lm}^{jm_j}(\mathbf{p}_0 | \hat{H}_1 | \psi_{l,m})$. Now the transition amplitude may be written

$$M(\mathbf{p}_f, z_f) = -i \sum_m \int_{-\infty}^{t'} dt' \mathcal{K}_m(\mathbf{p}_f, z_f) e^{-iE_{jm_j} t'}, \quad (27)$$

where

$$\mathcal{K}_m(\mathbf{p}_f, z_f) = \int d^3 \tilde{\mathbf{p}}_0 \langle \psi_{\mathbf{p}_f}(t), z_f | U(t, t') | \tilde{\mathbf{p}}_0, z_{lm}^{jm_j} \rangle d_m(\tilde{\mathbf{p}}_0, t'). \quad (28)$$

Now we are in a position to utilize the path-integral formalism for a particle with spin [84,86–88] and obtain

$$\begin{aligned} \mathcal{K}_m(\mathbf{p}_f, z_f) &= \int_{\mathbf{r}_0} \frac{\mathcal{D}'\mathbf{r}}{(2\pi)^3} \int^{\mathbf{p}_f} \mathcal{D}'\mathbf{p} \\ &\times \int_{z_{lm}^{jm_j}}^{z_f} \mathcal{D}\mu(z) d_m(\mathbf{p}_0, t') e^{iA[\mathbf{r}, \mathbf{p}, z, t']}, \end{aligned} \quad (29)$$

where

$$\begin{aligned} A[\mathbf{r}, \mathbf{p}, z, t'] &= - \int_{t'}^{\infty} d\tau \left(\dot{\mathbf{p}} \cdot \mathbf{r} + iS \frac{z\dot{z}^* - z^*\dot{z}}{1 + |z|^2} \right. \\ &\quad \left. + H[\mathbf{r}, \mathbf{p} + \mathbf{A}(\tau), z] \right) \end{aligned} \quad (30)$$

and

$$H[\mathbf{r}, \mathbf{p}, z] = K[\mathbf{p}] + U[\mathbf{r}] + \mathbf{C}_{\text{SO}}[\mathbf{r}, \mathbf{p}] \cdot \frac{\mathbf{n}[z]}{2}. \quad (31)$$

Here, $\mathbf{n}[z]$ is a semiclassical representation of \hat{S} , such that $\mathbf{n}[z] = (n_1, n_2, n_3)$, $n_1 + in_2 = 2z^*/(1 + |z|^2)$, and $n_3 = -(1 - |z|^2)/(1 + |z|^2)$. The kernel, given by Eq. (28), may be solved using the saddle-point approximation, however, a simpler solution is possible via the so-called weak approximation. The first step is to use the fact that the functional integral over z may be solved analytically. Rewriting Eq. (29) as

$$\begin{aligned} \mathcal{K}_m(\mathbf{p}_f, z_f) &= \int_{\mathbf{r}_0} \frac{\mathcal{D}'\mathbf{r}}{(2\pi)^3} \int^{\mathbf{p}_f} \mathcal{D}'\mathbf{p} \mathcal{M}_{\text{SO}}^m[\mathbf{r}, \mathbf{p}, z_f, t'] \\ &\times d_m(\mathbf{p}_0, t') e^{iA_{0,l}[\mathbf{r}, \mathbf{p}, t']}, \end{aligned} \quad (32)$$

where all spin and spin-orbit terms are collected in

$$\mathcal{M}_{\text{SO}}^m[\mathbf{r}, \mathbf{p}, z_f, t'] = \int_{z_{lm}^{jm_j}}^{z_f} \mathcal{D}\mu(z) e^{iA_{\text{SO}}[\mathbf{r}, \mathbf{p}, z, t']}. \quad (33)$$

Here,

$$A_{0,l}[\mathbf{r}, \mathbf{p}, t'] = - \int_{t'}^{\infty} d\tau (\dot{\mathbf{p}} \cdot \mathbf{r} + H_{0,l}[\mathbf{r}, \mathbf{p} + \mathbf{A}(\tau)]) \quad (34)$$

and

$$\begin{aligned} A_{\text{SO}}[\mathbf{r}, \mathbf{p}, z, t'] &= - \int_{t'}^{\infty} d\tau \left(iS \frac{z\dot{z}^* - z^*\dot{z}}{1 + |z|^2} \right. \\ &\quad \left. + H_{\text{SO}}[\mathbf{r}, \mathbf{p} + \mathbf{A}(\tau), z] \right), \end{aligned} \quad (35)$$

where $H_{0,l}[\mathbf{r}, \mathbf{p}] = K[\mathbf{p}] + U[\mathbf{r}]$ and $H_{\text{SO}}[\mathbf{r}, \mathbf{p}, z] = \mathbf{C}_{\text{SO}}[\mathbf{r}, \mathbf{p}] \cdot \mathbf{n}[z]$.

It is possible to solve Eq. (33) as [87]

$$\mathcal{M}_{\text{SO}}^m[\mathbf{r}, \mathbf{p}, z_f, t'] = \frac{a^*(t) - b^*(t)z_{lm}^{jm_j*} + b(t)z + a(t)z^*z_{lm}^{jm_j}}{\sqrt{1 + |z|^2} \sqrt{1 + |z_{lm}^{jm_j}|^2}}, \quad (36)$$

where $a(t)$ and $b(t)$ may be obtained by solving the following ordinary differential equation (ODE) [87]:

$$\begin{aligned} \dot{a} &= -\frac{i}{4c^2 r} \frac{dV}{dr} \{L_z(t)a - [L_x(t) - iL_y(t)]b^*\}, \\ \dot{b} &= -\frac{i}{4c^2 r} \frac{dV}{dr} \{L_z(t)b + [L_x(t) - iL_y(t)]a^*\} \end{aligned} \quad (37)$$

with $a(0) = 1$, $b(0) = 0$, and $\mathbf{L}(t) = \mathbf{r}(t) \times [\mathbf{p}(t) + \mathbf{A}(t)]$.

Now that we have a solution for $\mathcal{M}_{\text{SO}}^m[\mathbf{r}, \mathbf{p}, z_f, t']$, we may solve the remaining path integral with the saddle-point approximation, as in the spinless version. Here, we assume that $\mathcal{M}_{\text{SO}}^m[\mathbf{r}, \mathbf{p}, z_f, t']$ is a slowly varying function like $d_m(p, t')$ and treat it as a prefactor in the semi-classical approximation. This is a weak-coupling approximation, such as employed in Ref. [87], assuming that there is an effect of the trajectory motion on the spin but not vice versa, and will be valid if the spin-orbit action [Eq. (34)] is appreciably lower than the rest of the action. Thus, the final expression for the transition amplitude is given by

$$\begin{aligned} M(\mathbf{p}_f, z_f) &= -i \sum_{m,s} C_m(\mathbf{r}_s, \mathbf{p}_s, t_s) \mathcal{M}_{\text{SO}}^m \\ &\times (\mathbf{r}_s, \mathbf{p}_s, z_f, t_s) e^{iS[\mathbf{r}_s, \mathbf{p}_s, t_s]} \end{aligned} \quad (38)$$

with

$$C_m(\mathbf{r}_s, \mathbf{p}_s, t_s) = \sqrt{\frac{2\pi i}{\partial^2 S / \partial t'^2}} \frac{e^{-i\pi\nu/2}}{\sqrt{|J|}} d_m(\tilde{\mathbf{p}}_{0s}, t_s) \quad (39)$$

and

$$S[\mathbf{r}, \mathbf{p}, t'] = -E_{jm_j} t' - \int_{t'}^{\infty} d\tau (\dot{\mathbf{p}} \cdot \mathbf{r} + H_{0,l}[\mathbf{r}, \mathbf{p} + \mathbf{A}(\tau)]). \quad (40)$$

Note that this formulation assumes that $\mathcal{M}_{\text{SO}}^m$ varies slowly enough so that it does not affect the saddle-point equation for \mathbf{r}_s and \mathbf{p}_s , which is the weak-coupling limit. For details of how we may go beyond the weak approximation, see Appendix B.

V. OBSERVABLES AND ANALYTICAL CONSIDERATIONS

A. Spin measurement

So far we have only considered the case where the final spin is measured and the initial spins are aligned. Now we consider an ensemble of unaligned initial spins and the effect of averaging over final spins. We will use the notation $\mathcal{P}_{i,j}(\mathbf{p}_f)$ or $\mathcal{P}_i(\mathbf{p}_f; |j\rangle)$ for the probability amplitude given initial spin $j \in [\uparrow, \downarrow]$ and final spin $i \in [\uparrow, \downarrow]$ and momentum $\mathbf{p}_f \in \mathbb{R}^3$. For averages over initial, final, and both spins, we will use $\mathcal{P}_i(\mathbf{p}_f)$, $\mathcal{P}_{:,j}(\mathbf{p}_f)$, and $\mathcal{P}_{:,}(\mathbf{p}_f)$, respectively.

First, we will average incoherently over initial spin orientations, for simplicity we will continue with the case of hydrogen. In this case, the spin state $|\Phi_{0\pm 1/2}\rangle = |z_{00}^{\pm 1/2}\rangle |\psi_{00}(t')\rangle$, where either $z_{00}^{-1/2} \rightarrow 0$ (spin down) or $z_{00}^{+1/2} \rightarrow \infty$ (spin up).

Spatial rotations of the initial state can cover all possible values of the initial z_{00} . We can show this explicitly by integrating over the Euler angles

$$\mathcal{P}_{\uparrow;(\mathbf{p}_f)} = \frac{1}{8\pi^2} \int_0^{2\pi} d\alpha \int_0^\pi d\beta \int_0^{2\pi} d\gamma \times \sin(\beta) \mathcal{P}_{\uparrow}(\mathbf{p}; \mathcal{R}_{\alpha\beta\gamma} |\uparrow\rangle). \quad (41)$$

This is a well-known result but in Appendix C we show how to do this using coherent spin states, the result is

$$\mathcal{P}_{\uparrow;(\mathbf{p}_f)} = \frac{1}{2} [\mathcal{P}_{\uparrow;\uparrow}(\mathbf{p}_f) + \mathcal{P}_{\uparrow;\downarrow}(\mathbf{p}_f)]. \quad (42)$$

By the same logic $\mathcal{P}_{\downarrow;(\mathbf{p}_f)} = \frac{1}{2} [\mathcal{P}_{\downarrow;\uparrow}(\mathbf{p}_f) + \mathcal{P}_{\downarrow;\downarrow}(\mathbf{p}_f)]$.

If we do not measure spin, the positive operator-valued measurement (POVM) is given by $\rho = \frac{1}{2}(|\downarrow\rangle\langle\downarrow| + |\uparrow\rangle\langle\uparrow|)$. This may be applied to a state where the spins are initially prepared to give $\mathcal{P}_{;\uparrow} = \frac{1}{2}(\mathcal{P}_{\uparrow;\uparrow} + \mathcal{P}_{\downarrow;\uparrow})$ and $\mathcal{P}_{;\downarrow} = \frac{1}{2}(\mathcal{P}_{\uparrow;\downarrow} + \mathcal{P}_{\downarrow;\downarrow})$. If we instead apply the POVM to unaligned spins, we obtain the following probability: $\mathcal{P}_{;(\mathbf{p}_f)} = \frac{1}{2}[\mathcal{P}_{\uparrow;(\mathbf{p}_f)} + \mathcal{P}_{\downarrow;(\mathbf{p}_f)}] = \frac{1}{4}(\mathcal{P}_{\uparrow;\uparrow} + \mathcal{P}_{\uparrow;\downarrow} + \mathcal{P}_{\downarrow;\uparrow} + \mathcal{P}_{\downarrow;\downarrow})$.

To isolate the effect of spin, we define a parameter that could feasibly be measured in an experiment. This is $\Delta\mathcal{P}_{;\uparrow_x}(\mathbf{p}_f)$, defined as the difference between spin initially aligned in the x direction and unaligned spins given by the difference between spins aligned in the x direction vs fully unaligned spins, denoted $\mathcal{P}_{\uparrow_x}(\mathbf{p}_f)$ and $\mathcal{P}_{;(\mathbf{p}_f)}$, respectively. In the z basis these probabilities may be written as

$$\mathcal{P}_{;\uparrow_x}(\mathbf{p}_f) = \frac{1}{4} |M_{\uparrow_z;\uparrow_z}(\mathbf{p}_f) + M_{\uparrow_z;\downarrow_z}(\mathbf{p}_f)|^2 + \frac{1}{4} |M_{\downarrow_z;\uparrow_z}(\mathbf{p}_f) + M_{\downarrow_z;\downarrow_z}(\mathbf{p}_f)|^2 \quad (43)$$

and

$$\mathcal{P}_{;(\mathbf{p}_f)} = \frac{1}{4} (|M_{\uparrow_z;\uparrow_z}|^2 + |M_{\uparrow_z;\downarrow_z}|^2 + |M_{\downarrow_z;\uparrow_z}|^2 + |M_{\downarrow_z;\downarrow_z}|^2). \quad (44)$$

Now the difference can be expressed as

$$\begin{aligned} \Delta\mathcal{P}_{;\uparrow_x}(\mathbf{p}_f) &= \mathcal{P}_{;\uparrow_x}(\mathbf{p}_f) - \mathcal{P}_{;(\mathbf{p}_f)} \\ &= \frac{1}{2} \text{Re}[M_{\uparrow_z;\uparrow_z}(\mathbf{p}_f) M_{\uparrow_z;\downarrow_z}^*(\mathbf{p}_f)] \\ &\quad + \frac{1}{2} \text{Re}[M_{\downarrow_z;\uparrow_z}(\mathbf{p}_f) M_{\downarrow_z;\downarrow_z}^*(\mathbf{p}_f)]. \end{aligned} \quad (45)$$

This provides an ‘‘interference’’ term due to the fact that spin aligned in the x axis but we expressed in terms of the z basis. This provides an observable that is linear in terms of the spin-flip amplitude. The difference term in Eq. (45) may be written more clearly by expanding the transition amplitudes in terms of the sum over saddle points

$$M_{\uparrow_z;\uparrow_z} = -i \sum_s C_s a_s e^{iS_s}, \quad (46)$$

$$M_{\uparrow_z;\downarrow_z} = -i \sum_s C_s b_s e^{iS_s}, \quad (47)$$

where the subscript s refers to the saddle-point solution being summed over, the spin-orbit amplitude \mathcal{M}_{SO} [Eq. (36)] has been replaced by the coefficient a_s or b_s , while C_s is the prefactor defined in Eq. (39). The arguments \mathbf{p} , \mathbf{r} , t , and z have been dropped from a_s , b_s , and C_s for simplicity. Thus, the difference can be determined entirely by products of a and b . In the next section, we will solve the equations for a and b analytically to better understand the behavior of Eq. (45).

B. Analytical results

In this section we will consider some analytical results: First, we will solve the equations of motion for the spin dynamics and, second, derive an approximate analytic approximation to the spin-orbit action. As we are using the weak approximation in this work (see Sec. IV), the electron trajectories are unaffected by spin-orbit coupling and retain cylindrical symmetry. Furthermore, we restrict our analysis to the y - z plane, which means the trajectories will only have angular momentum in the x direction, with $L_z = L_y = 0$, the spin-orbit equations in the weak-coupling limit greatly simplify. The coefficients $a(t)$ and $b(t)$, that enter Eq. (36) and parametrize the spin dynamics [see Eq. (37)], can be found analytically (see Appendix D for derivation). The parameter responsible for spin-conserving transitions is given by

$$\begin{aligned} a(t) &= \cos(S_{\text{SO}}) \text{ and the parameter for spin flips,} \\ b(t) &= -i \sin(S_{\text{SO}}), \end{aligned} \quad (48)$$

where the term S_{SO} that we will refer to as the spin-orbit action is given by

$$S_{\text{SO}} = \int_{\text{Re}(t')}^t d\tau H_{\text{SO}}(\tau) \quad (49)$$

with

$$H_{\text{SO}}(\tau) = \mathbf{C}_{\text{SO}}(\mathbf{r}, \mathbf{p}) \cdot \frac{\mathbf{n}(z)}{2} \quad (50)$$

and

$$\mathbf{C}_{\text{SO}}(\mathbf{r}, \mathbf{p}) = \frac{\partial V(|\mathbf{r}|)}{2c^2 |\mathbf{r}|} \mathbf{L}. \quad (51)$$

Here $\mathbf{n}(z) = (n_1, n_2, n_3)$, $n_1 + in_2 = 2z^*/(1 + |z|^2)$, $n_3 = -(1 - |z|^2)/(1 + |z|^2)$, and $\mathbf{L} = \mathbf{r} \times \mathbf{p}$.

The weak-coupling approximation requires that the spin-orbit action S_{SO} is much smaller than the remaining action S . This means that a and b can be expanded in a power series of S_{SO} , such that $a(t) \approx 1$ and $b(t) \approx -iS_{\text{SO}}$. Hence, spin-flip probability will be quadratic in S_{SO} and may be neglected $|M_{\uparrow_z;\downarrow_z}|^2 \approx 0$ to linear order, which may be expected for the small spin-orbit coupling of hydrogen. However, the difference term given by Eq. (45) has mixed terms like ab^* and will be of linear order in S_{SO} and so some effect whereby different alignment of spin affects the final probability distribution is expected.

The spin-orbit action term S_{SO} can be accurately approximated by assuming contributions only occur when the trajectory is very close to the origin and undergoing Coulomb dominated dynamics (see Fig. 3). Thus, during the recollision it is an accurate approximation to neglect the laser field and assume the trajectories follow Kepler hyperbola, or when including relativistic corrections to the kinetic energy, the trajectories will follow relativistic corrected Kepler hyperbola [89], which for a $-Z/r$ potential takes the form

$$\frac{1}{r} = \bar{C}_0 \{1 + \bar{e} \cos[\bar{\kappa}(\theta - \theta_c)]\}, \quad (52)$$

where $\bar{C}_0 = (1 + \frac{1}{2}\epsilon)(Z/l^2)$, $\bar{\kappa} = 1 - \frac{1}{2}\epsilon$, with the corrected eccentricity $\bar{e} = (1 + \frac{1}{2}\epsilon)e$ written in terms of the Kepler eccentricity $e = \sqrt{1 + 2El^2/Z^2}$, with E being the energy and l

the magnitude of the angular momentum in the nonrelativistic case. The relativistic correction parameter $\epsilon = 1/(\bar{l}^2 c^2)$, where the magnitude of the relativistic angular momentum $\bar{l} \approx l(1 + v^2/c^2)$. In the case without relativistic corrections to the kinetic energy $\epsilon = 0$. The spin-orbit action S_{SO} , given in Eq. (49), may be written more explicitly as

$$S_{\text{SO}} = \frac{Z}{2c^2} \int_{\text{Re}[t']}^t \frac{\bar{l} d\tau}{r^3} \quad (53)$$

by substituting the integration variable from time t to the orbital angle θ via $r^2 d\theta = \bar{l} d\tau$ and substituting in Eq. (52) the spin-orbit action can be approximated as

$$S_{\text{SO}} \approx \frac{\bar{C}_0}{2c^2} \left[\arccos\left(-\frac{1}{\bar{e}}\right) + \frac{\bar{e}}{\bar{\kappa}} \sqrt{1 - \frac{1}{\bar{e}^2}} \right]. \quad (54)$$

This equation is tested in Fig. 3, using the position and velocity when the recolliding trajectory first reaches a distance of 1 a.u. from the residual ion, the value of the spin-orbit action phase S_{SO} is computed and placed on the figure as the circles in Figs. 3(c) and 3(f). This works exceptionally well for the nonrelativistic case [Fig. 3(c)], with no difference visible between it (colored circle) and the numerical value (dotted-dashed line). It also works well for the case including relativistic correction to the kinetic energy [Fig. 3(f)], however, the approximated value (represented by a circle) is slightly off the numerical value (plotted as a dotted-dashed line), indicating the analytical estimation slightly worsens in the relativistic case.

VI. RELATIVISTIC RESULTS

The trajectories involved in the relativistic computation are shown in the bottom row of Fig. 3. With relativistic corrections to the kinetic energy, the velocity of the rescattered trajectories [Fig. 3(d)] no longer exceeds the speed of light. There is also a directly related effect on the minimum distance to the core [Fig. 3(e)], which is increased by more than two orders of magnitude compared to the nonrelativistic case in Fig. 3(b). We can gain insight into why the core is probed less strongly when relativistic corrections are included by examining the problem from a nonrelativistic perspective. We may imagine that there is an effective “repulsion” (dependent on the velocity), which balances the attraction of the Coulomb potential, meaning that the electron does not get so close to the core, only reaching around 10^{-3} a.u. This effect can be seen clearly by rearranging the saddle-point equations of motion (neglecting the laser field) to give

$$\ddot{\mathbf{r}} = \left(\mathbb{1}_3 - \frac{1}{2c^2} \underline{\underline{M}} \right) \mathbf{F}, \quad (55)$$

where $\mathbf{F} = -\nabla V(\mathbf{r})$ is the classical nonrelativistic force due to the potential and $\underline{\underline{M}}$ is a matrix given by $\underline{\underline{M}} = \mathbb{1}_3 \mathbf{p}^2 + 2\mathbf{p} \otimes \mathbf{p}$. For a derivation of Eq. (55), see Appendix E. Now it is possible to see, following Appendix E, that for a trajectory with momentum \mathbf{p} confined to the z axis, the attractive force of the potential is reduced by the factor $1 - \frac{3}{2} \frac{v^2}{c^2}$, while for circular

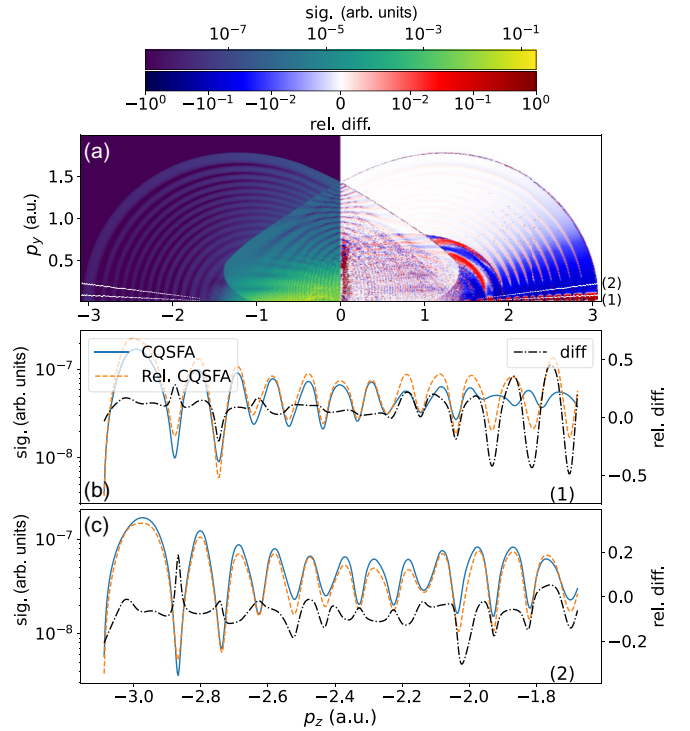


FIG. 5. The difference between momentum distributions with and without relativistic corrections. Spin and spin-orbit effects have been neglected by setting the $\mathcal{M}_{\text{SO}} = 1$ in Eq. (38). (a) Left is the relativistic momentum distribution for a hydrogen target. (a) Right is the difference between this and the distribution without relativistic corrections to the kinetic energy. (b), (c) Include a line out of (a) left (solid and dashed lines) and (a) right (dotted-dashed line), given by the lower [labeled (1), (b)] and upper [labeled (2), (c)] white lines in (a), respectively.

motion with momentum perpendicular to the origin this factor becomes $1 - \frac{1}{2} \frac{v^2}{c^2}$. In both cases, this leads to trajectories that do not probe the core as closely as in the nonrelativistic case. The result of the significant increase in the minimal distance from the core and the reduction in the velocity is that the spin-orbit action phase term is greatly reduced by an order of magnitude for the directly recolliding trajectory pairs, and by over a factor of 5 for the long and short trajectory pairs, and these phases for all trajectories are over an order of magnitude below the phase due to the Coulomb potential. Thus, without relativistic corrections to the kinetic energy, the spin-orbit coupling phase is overestimated by around an order of magnitude, while with relativistic corrections, spin-orbit coupling is quite modest. The relatively small action phase of the spin-orbit coupling, in this case, also validates the weak-coupling approach used in the relativistic CQSFA of Sec. IV.

Another important observation that was already discussed in Sec. V is that the analytical approximation for the spin-orbit phase, given by Eq. (54), provides a very good approximation when compared to the numerical value, in Figs. 3(c) and 3(f), for the case without and with the kinetic energy corrections, respectively.

In Fig. 5, we show the PMD for a linearly polarized monochromatic laser field, where ionization is allowed only during a single cycle. The target is hydrogen as before and

the intensity and wavelength are again 5×10^{13} W/cm² and 1600 nm, respectively. The consideration of a single cycle provides a simple PMD, with fewer trajectories for an easier analysis, while also maximizing the rescattered trajectories' return energy, thus showing the largest relativistic effects. Similar results can still be seen for relativistic computations using a \sin^2 envelope (not shown). In this figure, we have neglected the spin and spin-orbit effect to isolate the kinetic energy corrections $K_1(\hat{\mathbf{p}})$ in Eq. (16). The left side of Fig. 5(a) plots the PMD including relativistic corrections to the kinetic energy, where the same high-energy rings (p_{fz}, p_{fy}) \approx $(-3.0, 0.1)$ a.u. can be seen as in Fig. 2(a). The right side of Fig. 5(b) shows the normalized difference between the CQSFA with and without relativistic kinetic energy corrections. We find that in the high-energy rescattering region near the p_z axis a series of peaks occur, which shows that the CQSFA PMD signal with relativistic kinetic energy corrections is larger than without. However, away from the p_z axis this situation reverses. In Figs. 5(b) and 5(c), we look at these regions in more detail by plotting the line outs, marked on Fig. 5(a). The first line out, near the axis Fig. 5(b), clearly shows that the relativistic case exceeds the nonrelativistic case, with the normalized difference exceeding 50%. While the situation is reversed in Fig. 5(c) and the normalized difference approaches 20%.

The main driver of this effect is an overall change in probability for the pair of rescattered trajectories that contribute to this region. This is because scattering with and without relativistic corrections only appreciably changes $\mathbf{p}_{0\perp}$, the initial momentum perpendicular to the laser polarization direction, while the ionization times and tunneling probability remain almost the same. The case with relativistic corrections leads to a larger value of initial perpendicular momentum $|\mathbf{p}_{0\perp}|$ than the nonrelativistic case. The perpendicular momentum controls how close the electron trajectory gets to the ion, with a higher value meaning the core gets probed less strongly, as is the case with relativistic corrections.

These changes in initial conditions affect the so-called stability factor $1/\sqrt{|J|}$, determined from the Jacobian by $J = \frac{\partial \mathbf{p}_f}{\partial \mathbf{p}_0}$ in Eq. (8) [see also Eq. (39)], which leads to the visible changes in the PMDs. The stability factor is inversely proportional to the sensitivity trajectories to initial conditions, hence, it acts to suppress chaotic-style trajectories that are very sensitive to initial conditions. In the case of backscattering, where the scattering angle is nearly 180° , the trajectories for the case including relativistic kinetic energy corrections undergo a much smaller momentum change than those without the kinetic energy corrections. This means they are less sensitive to the initial conditions, hence, the relativistic case is more probable. On the other hand, for scattering angles less than approximately 175° , the trajectories including relativistic corrections have a comparable momentum transfer to those without the corrections. However, in this case the relativistic scattering leads to greater sensitivity to the initial conditions than the case without corrections. Hence, for these scattering angles the relativistic case is a lower in probability, as compare to no kinetic energy corrections.

Now we will consider the effect of spin-orbit coupling. It is important to note that in this article we only consider the final electron momentum in the p_{fz} - p_{fy} plane, and the equations of

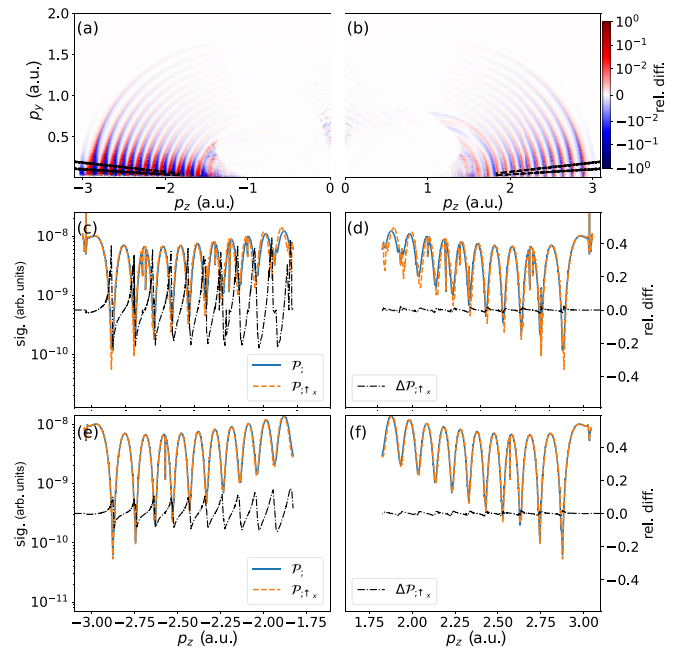


FIG. 6. The difference between momentum distributions with initial spin aligned in the x direction and fully averaged spins, given by $\Delta\mathcal{P}_{i\uparrow x}(\mathbf{p})$ defined in Eq. (45). The left column [(a), (c), (e)] neglects the corrections to the kinetic energy, the right column [(b), (d), (e)] includes corrections to the kinetic energy. (a), (b) Show the relative difference over the full momentum region. The line outs, given by the two nearly horizontal black lines in (a) and (b), show the signal of averaged spins $\mathcal{P}_i(\mathbf{p}_f)$ and x -aligned spins $\mathcal{P}_{i\uparrow x}(\mathbf{p}_f)$, and relative difference $\Delta\mathcal{P}_{i\uparrow x}(\mathbf{p}_f)$. As in Fig. 5, the lower line out in (a) [(b)] corresponds to (c) [(d)], while the upper line out corresponds to (e) [(f)]. Note, “sig. arb. units” (signal arbitrary) refers to the signal of the momentum-based probability density; here the overall value is arbitrary as we only interested in the relative difference between $\Delta\mathcal{P}_{i\uparrow x}(\mathbf{p})$ and $\mathcal{P}_i(\mathbf{p}_f)$.

motion for the electron are cylindrically symmetric.² Thus, the trajectories are restricted to the zy plane, and the angular momentum is in the x direction and couples to spin in this direction. For motion in rotated planes, e.g., the p_z - p_x plane, the angular momentum and spin-orbit coupling will be rotated accordingly.

In Fig. 6, the effect of spin-orbit coupling is considered on the initial alignment of the electronic spin. Figure 6(a) shows the relative difference between electronic spin aligned in the positive x direction vs unaligned spins, where relativistic kinetic energy corrections have been neglected. This combination of spin alignment is considered, as it could be feasibly done in experiment and measured, using a B field for spin alignment. Line outs near the p_z axis are shown in Figs. 6(c) and 6(e) (the same as in Fig. 5, where the largest effect, due to the backscattered trajectories, can be observed). Here, the relative difference approaches 50%; this is surprising given the small degree of spin-orbit coupling expected for

²This is because, in the weak-coupling limit, the effect of spin-orbit coupling on the electronic motion is neglected.

a hydrogenic target, and this difference could foreseeably be measured.

As argued above, a correct treatment requires that corrections to the kinetic energy be taken into account, so we plot the same in Figs. 6(b), 6(d), and 6(f) but include these corrections. This leads to much weaker differences, demonstrating the importance of including the relativistic kinetic energy correction for the rescattered electron when considering spin-orbit coupling. The difference with and without the relativistic kinetic energy corrections can be explained by the behavior of the spin-orbit phase, which is far too big if kinetic energy corrections are not taken into account (see Fig. 3).

VII. NEW LIMIT ON NONRELATIVISTIC THEORIES

The results from Sec. VI highlight the importance of relativistic corrections for the rescattered portion of the wave packet in strong-field ionization. However, commonly employed estimations for when relativistic effects should be accounted for in the infrared regime rely on classical arguments considering the motion of the free electron in the continuum [27,82] and do not account for scattering. In this section, limits will be derived that account for the scattering behavior and we will compare to existing limits.

A commonly employed limit for relativistic behavior is when the ponderomotive energy approaches the electron rest mass energy, that is $U_p = mc^2/2$ [82]; this leads to a condition on the intensity $I_0 = 2c^2\omega^2$ above which relativistic effects are significant. This is plotted as dashed line in the upper left corner of Fig. 7(b), and the dot, which indicates the parameters used here, is well below this intensity. Another important condition is the region where the dipole approximation is valid; this is given by an “upper” and “lower” limit. The “upper” limit is simply that the angular frequency needs to be small enough and is given by $\omega = \frac{1}{2}$ [82]. The “lower” limit derives from the requirement that the motion of the free electron due to the laser magnetic field should be small and leads to the following limit on intensity $I_0 = 8c\omega^3$, where higher intensities mean the breakdown of the dipole approximation. These upper and lower limits are given by the solid red lines making a triangle in Fig. 7(b). A slightly smaller triangle region, where tunneling models will hold, is also given by the blue dotted lines in Fig. 7(b) (see [82]).

Here we derive a new condition, using the maximum velocity that a classical rescattering trajectory would achieve given specific laser parameters and particular scattering angle. We will consider angles close to backscattered, as these represent the most extreme cases. In the Coulomb-free case, the most energetic rescattered trajectories gain around $3.17U_p$ kinetic energy from the laser field upon return. If we assume once the electron is close enough, r_B from the core, it undergoes Coulomb dominated dynamics, and we may ignore the field from this point, then an energy conservation argument may be used to approximate the maximum velocity. The total energy entering this boundary may be approximated as $E_B = 3.17U_p - Z/r_0$, where the potential energy converted to kinetic energy from the tunnel exit at r_0 to the boundary (r_B) has also been accounted for. Equating E_B with the energy at closest approach r_m gives an equation for the maximum

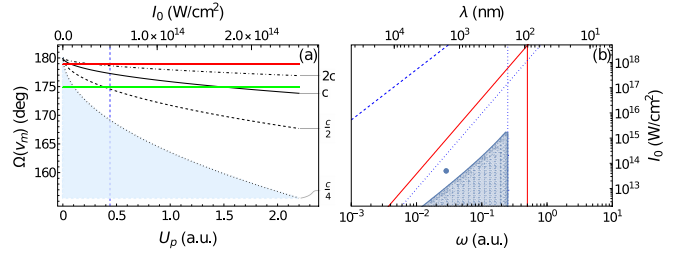


FIG. 7. The limits of a nonrelativistic theory for rescattered photoelectrons. (a) The scattering angle $\Omega(v_m)$ for particular maximum rescattering velocities ($v_m = c/4$, $c/2$, c , and $2c$, given by the dotted, dashed, solid, and black dotted-dashed curves, respectively) across a range of intensities, as given by Eq. (61). The shaded region below the curve for $v_m = c/4$ is the region where relativistic effects will not play a role. The wavelength (angular frequency) is fixed to 1600 nm (0.0285 a.u.), the upper (red) and lower (green) horizontal lines denote a 179° and 175° scattering angle, respectively. The dashed vertical line (in blue) denotes the intensity of $I_0 = 5 \times 10^{13}$ W/cm² ($U_p = 0.44$ a.u.), used in this study. (b) For a range of angular frequencies and intensities, the region where a nonrelativistic theory holds for the rescattered photoelectrons is given by the shaded region, as given by Eq. (61). This assumes a maximum scattering velocity of $0.25c$ and a maximum scattering angle of 175° . The dashed blue line in the top left of the figure denotes the typical relativistic condition $I_0 = 2c^2\omega^2$, while the solid triangle (red) denotes the dipole conditions $\omega = \frac{1}{2}$ and $I_0 = 8c\omega^3$, outside of which the dipole approximation breaks down. Similarly, the inner dotted (blue) triangle marks the region where a tunneling model will hold, $\omega = \frac{1}{4}$ and $I_0 = 2c\omega^3$, as given in [82]. A solid (blue) circle is used to show the parameters used in this study, which lies just outside of the shaded region.

velocity

$$\frac{1}{2}v_m^2 = E_B + \frac{Z}{r_m}; \quad (56)$$

assuming Coulomb dominated dynamics we may substitute the equation for a Kepler hyperbola at the closest approach [see Eq. (52)],

$$\frac{1}{2}v_m^2 = E_B + \frac{Z^2}{l^2}(1 + e), \quad (57)$$

where for nearly backscattered trajectories $e \approx 1$

$$\frac{1}{2}v_m^2 = E_B + \frac{2Z^2}{l^2}. \quad (58)$$

Now the angular momentum may be written in terms of the maximal velocity

$$l^2 = \frac{4Z^2}{V_m^2 - 2E_B}. \quad (59)$$

The dynamics will depend on the scattering angle, the closer to backscattering the higher the maximum velocity will be. Thus, we can use the scattering angle to help formulate the condition. The scattering angle $\Omega = 2\Psi - \pi$, where Ψ is the asymptote angle, that is the angle between the direction of the incoming asymptotic and closest approach (periapsis)

direction, which is given by

$$\cos \Psi = -\frac{1}{\sqrt{1 + \frac{2E_B I^2}{Z^2}}}. \quad (60)$$

Inserting Eq. (59) gives an equation for the scattering angle in terms of the maximal velocity

$$\Omega(v_m) = 2 \arccos \left(-\frac{1}{\sqrt{1 + \frac{8E_B}{v_m^2 - 2E_B}}} \right) - \pi. \quad (61)$$

In Fig. 7(a), contours of Eq. (61) are given for different values of v_m in terms of c . For an increasing laser intensity, the scattering angle (given a fixed maximal velocity) reduces. For the curve $\Omega(c/4)$, this is used to denote a region (shaded in blue), where relativistic effects may be neglected. As intensity increases, this region reduces so that less of the rescattered wave packet may be accurately described by a nonrelativistic model, as higher velocities will be reached during rescattering. The parameter region in this study (dashed vertical line), crosses this boundary for scattering angle greater than 170° , and crossed the $\Omega(2c)$ at around 179° . This is confirmed by Fig. 3, where the long and short orbit 4 trajectories scattered by 179° reach velocities just over $2c$, when neglecting corrections to the kinetic energy. Note that orbit 4b would actually require a stronger condition, as it has a return energy of higher than E_B and returns with a $6c$ velocity. However, for these parameters, this solution has low probability.

In Fig. 7(b), we use this condition to construct a modified region (shaded region) inside the dipole-allowed region, where relativistic effects are not important for scattering angles $\Omega(0.25c) < 175^\circ$, given a maximal velocity of $v_m = 0.25c$. This reduces the standard dipole allowed region by around a factor of 2, and the dot representing the parameters used in this study lies outside this region despite being inside the dipole-allowed region. Note, the typical relativistic condition (blue dashed line in the upper left of the figure) lies more than six orders of magnitude in intensity from our modified condition, demonstrating the huge difference that rescattering can make when considering relativistic effects.

VIII. CONCLUSION AND OUTLOOK

Driving atomic and molecular systems with near-infrared light at intensities up to around 10^{14} W/cm² was thought to be well described by nonrelativistic quantum mechanics [82], aside from effects associated with large spin-orbit energy splitting in the cationic system [58]. In this study, we have used the powerful machinery of the path-integral-based CQSFA to investigate spin-orbit coupling and other relativistic dynamics in more detail. For the parameter range explored, we find the CQSFA provides an exceptional quantitative agreement with the single-active electron TDSE. However, upon close inspection, we have illustrated that the nonrelativistic and relativistic treatments deviate for a significant portion of the rescattered electron wave packet, at a laser intensity orders of magnitude below that expected. The origin of this deviation may be interpreted via the CQSFA, where

backscattered trajectories probe the core very closely and gain significant kinetic energy.

We present an extended CQSFA to include all relativistic correction terms from the Breit-Pauli Hamiltonian, including spin-orbit coupling and corrections to the kinetic energy. With this improved model we evaluate the effects of these terms, and find the kinetic energy corrections to be significant for the rescattered part of the electron, while the spin-orbit coupling is massively overestimated if computed without the former. Accordingly, the assessment of dynamical spin-orbit effects by theory not accounting for relativistic kinetic energy corrections (which is common given its inclusion is numerically intensive) need to take care since such theory would significantly overestimate the spin-orbit interaction effects. In order to inform future work, we provide an expression for where relativistic effects become important, which lies many orders of magnitude below the typical limit for relativistic effects.

The rescattered region in question is important for application in attosecond physics and chemistry, through imaging processes, such as LIED, where the diffraction pattern of the rescattered electron is used to infer subfemtosecond nuclear motion in molecules [90,91]. Clearly, an interpretation of an experimental PMD with a model involving nonrelativistic cross sections would lack the spin-orbit and kinetic energy corrections of focus in this work, and could therefore lead, e.g., to deviations between inferred and actual time-resolved distances. Thus, the models used for LIED should incorporate relativistic scattering cross sections. Work assessing quantitatively the implications of our findings for this kind of investigation is currently in progress, including adapting the CQSFA for LIED.

The conclusions and perspectives discussed above were obtained from the theory developments of this work, where an improved nonrelativistic quantum trajectory-based CQSFA was used to reach greatly improved agreement with TDSE simulations for PMDs. This agreement allowed us to proceed with a relativistic extension of the CQSFA. The coherent spin formalism and weak-coupling limits allowed such development, including analytical elucidation of the dynamics. The trajectory-based approach benefits from ease of interpretation in terms of possibly interfering quantum paths. Furthermore, the effects of the different coupling terms in the action can easily be isolated. This separation into individual contributions was used here to show the reduction in the spin-orbit action phase by the corrections to the relativistic energy. Such methodologies could also be extended to describe the spin of a residual ion. Furthermore, the coherent spin state formalism opens up the possibility of including other degrees of freedom supported by this description, such as the quantum state of the laser, which has recently been found to lead to a broad range of significant effects [92–98].

Looking into the future, it would be very interesting to connect this work with recent work on orbital angular momentum in strong-field ionization [99–101] and examine the role of total angular momentum in imaging, as well as the implications for inelastic recollision and double-ionization processes [102] demonstrating angular momentum entanglement. Another important direction is to extend the present studies to longer mid-infrared wavelengths, say up to around 3000 nm. This is

the wavelength regime of current LIED experiments [90,91]. The present CQSFA with relativistic corrections is scalable to this wavelength domain, while TDSE-based approaches would be severely challenged by numerical difficulties related to the increase in the required number of total angular momenta, along with relativistic corrections. In this longer-wavelength regime, nondipole corrections to the laser-matter interaction would have to be included [82,103], and this will affect the initial conditions for the trajectories [104], as well as the shape of the PMD and ATI [105,106]. In fact, nondipole effects have been shown to have some measurable effects at wavelengths and intensities comparable to this study [107–109].

In addition to the scaling with wavelength, our results also show that the interval of backscattering angles, where relativistic corrections are needed, increases with laser intensity. Mid-infrared intense femtosecond laser pulses are currently becoming more readily accessible, e.g. [110], so we envision increased need for theory incorporating relativistic effects in the future. If the rescattering energy becomes sufficiently large, one could even contemplate laser-induced time-resolved investigations of the structure of the atomic nucleus, with an achievable timescale of less than an attosecond made possible by the very brief electron transit, opening up a new domain on subattosecond physics.

ACKNOWLEDGMENTS

A.S.M. acknowledges funding support from the European Union's Horizon 2020 research and innovation programme under the Marie Skłodowska-Curie Grant Agreement No. SSFI No. 887153. L.B.M. acknowledges support from the Danish Council for Independent Research (Grants No. 9040-00001B and No. 1026-00040B).

APPENDIX A: CQSFA THEORY

In this Appendix, we discuss some additional approximations that are used in the CQSFA theory. We use the analytical Kepler expression to extend the trajectories and action asymptotically to infinite time, once the laser pulse is over [74,111]. The tunnel integral over the binding potential is approximated by the Coulomb factor [112,113],

$$\exp\left(i \int_{t_s}^{\text{Re}(t_s)} V[\mathbf{r}_s(\tau)] d\tau\right) \approx \left(\frac{4I_p}{|\mathbf{E}(t_s)|}\right)^{\frac{z}{\sqrt{2}p}}. \quad (\text{A1})$$

This approach has two advantages: it automatically regularizes the divergent integral, given by direct evaluation of the integral in Eq. (A1), and avoids branch cuts that arise in this integral, due to taking the square root of the complex-valued position vector over the tunnel exit. As in previous works [61–63], we take the position to be real for real-time propagation, i.e., $\mathbf{r}_s[\text{Re}(t_s)] = \text{Re}(\mathbf{r}_0)$ and keep the momentum fixed during tunneling, i.e., $\mathbf{p}_s(t) = \mathbf{p}_{0s}$ for $t \in [t_s, \text{Re}(t_s)]$. Here, the tunnel exit is given by

$$\mathbf{r}_0 = \text{Re}\left(\int_{t_s}^{\text{Re}(t_s)} d\tau [\mathbf{p}_{0s} + \mathbf{A}(\tau)]\right). \quad (\text{A2})$$

Aside from these approximations specifying the initial conditions for the trajectory propagation, all other parts of the action, given by Eq. (7), are computed in full.

APPENDIX B: MODIFIED SADDLE-POINT APPROXIMATION

In this Appendix we present a derivation of a modified saddle-point approximation that could be used for cases of strong spin-orbit coupling. We did not use the modified saddle-point approximation in the main text because it is significantly more complex than the weak-coupling approximation, which is valid for the case of hydrogen.

The weak approximation requires that the action for spin-orbit coupling is significantly less than the remaining action. However, instead it is possible to apply the saddle-point approximation to the full path integral, which allows its use for systems with higher spin-orbit coupling, e.g., for larger atoms. This has been called the extended phase-space formulation [87], as it treats the real and imaginary parts of the coherent spin state coefficient like an extra component of position and momentum. Although this formalism has the potential to be quite powerful and descriptive, there were a number of reasons that we did not use it in the main text. First, it breaks the cylindrical symmetry of the equations of motion: this means simplifications that exploit this can not be used, making the calculation more numerically intensive. Second, the computation of the fluctuation factor (B2) is nontrivial and goes beyond the scope of this work. Finally, for strong-field ionization of hydrogen, the weak approximation remains valid and can be very simply expressed as a prefactor term. Hence, to derive the modified saddle-point approximation, we evaluate Eq. (29) directly via the saddle-point approximation, leading to

$$M(\mathbf{p}_f, z_f) = \sum_{m,s} \sqrt{\frac{2\pi i}{\partial^2 S / \partial t^2}} \mathcal{F} d_m(\tilde{\mathbf{p}}_{0s}, t_s) e^{iS[\mathbf{r}_s, \mathbf{p}_s, z_s, t_s]}. \quad (\text{B1})$$

This expression is very similar to that in Eq. (33), except here the saddle points are different, and the fluctuation factor \mathcal{F} can be determined by

$$\mathcal{F} = \int \mathcal{D}[\boldsymbol{\eta}] \exp(i\mathcal{A}^{(2)}[\boldsymbol{\eta}]), \quad (\text{B2})$$

where $\boldsymbol{\eta} = (\delta\mathbf{r}, \delta v, \delta\mathbf{p}, \delta u)$ (given $z = u - iv$), which is known as the extended phase-space vector of small variations [84]. The second variation of the action is given by

$$\mathcal{A}^{(2)}[\boldsymbol{\eta}] = \frac{1}{2} \left(\boldsymbol{\eta} \cdot \Gamma \dot{\boldsymbol{\eta}} - \boldsymbol{\eta} \cdot \frac{\partial^2 H}{\partial \boldsymbol{\eta} \partial \boldsymbol{\eta}} \boldsymbol{\eta} \right), \quad (\text{B3})$$

where $\Gamma = \begin{pmatrix} 0 & \mathbb{1}_4 \\ -\mathbb{1}_4 & 0 \end{pmatrix}$ (known as the eight-dimensional unit symplectic matrix), with $\mathbb{1}_4$ being the four-dimensional identity matrix. The saddle-point equations are given by

$$\dot{\mathbf{r}} = \frac{\partial H}{\partial \mathbf{p}} = \mathbf{p} + \mathbf{A}(\tau) + \mathbf{C}_{\text{so}}[\mathbf{r}, \mathbf{n}[z]], \quad (\text{B4})$$

$$\dot{\mathbf{p}} = -\frac{\partial H}{\partial \mathbf{r}} = -\nabla U(\mathbf{r}) - \frac{1}{|\mathbf{r}|} \mathbf{C}_{\text{so}}[|\mathbf{r}|\mathbf{n}[z], \mathbf{p}], \quad (\text{B5})$$

while the equations for \dot{z} use $z = u - iu$,

$$\dot{u} = (1 + |z|^2)^2 \frac{1}{2} \frac{\partial H}{\partial u} = \mathbf{C}_{\text{SO}}[\mathbf{r}, \mathbf{p}] \cdot \begin{pmatrix} 1 - u^2 + v^2 \\ -2uv \\ 2u \end{pmatrix}, \quad (\text{B6})$$

$$\dot{v} = (1 + |z|^2)^2 \frac{1}{2} \frac{\partial H}{\partial v} = \mathbf{C}_{\text{SO}}[\mathbf{r}, \mathbf{p}] \cdot \begin{pmatrix} -2uv \\ 1 + u^2 - v^2 \\ 2v \end{pmatrix}, \quad (\text{B7})$$

which provides equations of motion for the spin. This is an alternative to what was used in the main text, where the spin-orbit coupling did not affect the equations of motion for the electron trajectories. Now the position, momentum, and spin are determined by coupled equations. This provides a very flexible formalism to describing spin through a path integral and connect it to semiclassical equations of motion, which can provide crucial insight into the dynamics. This could also be applied to describe the spin of the residual ion, where for a multielectron description a higher-dimensional representation of the coherent spin state can be used. Such a description is not restricted to spin, and a similar formalism could potentially be used to incorporate the quantum state of the light field via a coherent state path integral.

APPENDIX C: SPIN AVERAGING

We may use the coherent spin state formalism to average incoherently over initial spin orientations; for hydrogen, we use the spin state $|\Phi_{1/2\pm 1/2}\rangle = |z_{00}^{1/2\pm 1/2}\rangle |\psi_{00}(t')\rangle$, where either $z^{1/2\pm 1/2} \rightarrow 0$ (spin down) or $z^{1/2\pm 1/2} \rightarrow \infty$ (spin up). The state $|\psi_{00}(t')\rangle$ indicates that the spatial part is initially in an s state with $l = m = 0$. Spatial rotations to the initial state mean that all possible values of initial z_{00} will be covered. We can show this explicitly by integrating over the Euler angles [see Eq. (41) of the main text]

$$\mathcal{P}_{\uparrow}(\mathbf{p}_f) = \frac{1}{8\pi^2} \int_0^{2\pi} d\alpha \int_0^\pi d\beta \int_0^{2\pi} d\gamma \sin(\beta) \times \mathcal{P}_{\uparrow}(\mathbf{p}_f; \mathcal{R}_{\alpha\beta\gamma} |\uparrow\rangle). \quad (\text{C1})$$

Parametrizing the rotating as $\mathcal{R}_{\alpha\beta\gamma} = \exp(-i\alpha\sigma_z/2) \exp(-i\beta\sigma_y/2) \exp(-i\gamma\sigma_z/2)$, we may write the rotation of the spin-up state as

$$\mathcal{R}_{\alpha\beta\gamma} |\uparrow\rangle = e^{i\gamma/2} [e^{-i\alpha/2} \cos(\beta/2) |\uparrow\rangle + e^{i\alpha/2} \sin(\beta/2) |\downarrow\rangle]. \quad (\text{C2})$$

This may be written in terms of coherent spin states

$$\mathcal{R}_{\alpha\beta\gamma} |\uparrow\rangle = e^{i\alpha/2 - i\gamma/2} |e^{-i\alpha} \cot(\beta/2)\rangle. \quad (\text{C3})$$

We may drop the phasor prefactors as these will not contribute in the incoherent average, which may be written as

$$\mathcal{P}_{\uparrow}(\mathbf{p}_f) = \frac{1}{8\pi^2} \int_0^{2\pi} d\alpha \int_0^\pi d\beta \int_0^{2\pi} d\gamma \times \sin(\beta) \mathcal{P}_{\uparrow}[\mathbf{p}_f; |e^{-i\alpha} \cot(\beta/2)\rangle] \quad (\text{C4})$$

$$= \frac{1}{4\pi} \int_0^{2\pi} d\alpha \int_0^\pi d\beta \sin(\beta) \mathcal{P}_{\uparrow} \times [\mathbf{p}_f; |e^{-i\alpha} \cot(\beta/2)\rangle]. \quad (\text{C5})$$

As there is no γ dependence we could do the γ integral directly. To continue, we make the variable transformation $\phi_0 = -\alpha$ and $u_0 = \cot(\beta/2)$. The u_0 integration metric can be written as $du_0 = -\frac{d\beta}{2 \sin(\beta/2)^2}$, which means that $d\beta \sin(\beta) = -\frac{4u}{(1+u^2)^2}$. This means the averaged probability may be written as

$$\mathcal{P}_{\uparrow}(\mathbf{p}_f) = \frac{1}{\pi} \int_0^{2\pi} d\phi_0 \int_0^\infty u_0 du_0 \frac{1}{(1+u_0^2)^2} \mathcal{P}_{\uparrow}(\mathbf{p}_f; |u_0 e^{i\phi_0}\rangle) \quad (\text{C6})$$

$$= \frac{2}{\pi} \int_{\mathbb{C}} d^2 z_{00} \frac{1}{(1+|z_{00}|^2)^2} \mathcal{P}_{\uparrow}(\mathbf{p}_f | z_{00}), \quad (\text{C7})$$

where we have let $z_{00} = u_0 e^{i\phi_0}$ with $dz_{00}^2 = dz_{00} \wedge dz_{00}^* = 2i u_0 du_0 \wedge d\phi_0$ leading to the integral over the coherent spin states.

Now we can compute the spin average using Eq. (C7). We may write the probability given an initial z_{00} and final spin up using the weak-coupling formalism, but without actually applying any approximation, so it is still exact. The probability is given by

$$\mathcal{P}_{\uparrow}(\mathbf{p}_f; z_{00}) = \left| \int_{-\infty}^{\infty} dt' \int \mathcal{D}\mathbf{r} \int \frac{\mathcal{D}\mathbf{p}}{(2\pi)^3} \mathcal{M}_{\text{SO}}^{\uparrow}[\mathbf{r}, \mathbf{p}, t'; z_{00}] \times d(\mathbf{p}_0, t') e^{iS_{0,1}[\mathbf{r}, \mathbf{p}, t']} \right|^2. \quad (\text{C8})$$

Only the term $\mathcal{M}_{\text{SO}}^{\uparrow}[\mathbf{r}, \mathbf{p}, t'; z_{00}]$ contains dependence on z'_{00} from Eq. (36) this term may be written as

$$\mathcal{M}_{\text{SO}}^{\uparrow}[\mathbf{r}, \mathbf{p}, t'; z_{00}] = \frac{b + az_{00}}{\sqrt{1 + |z_{00}|^2}}, \quad (\text{C9})$$

similarly for $\mathcal{M}_{\text{SO}}^{\downarrow}$ we have

$$\mathcal{M}_{\text{SO}}^{\downarrow}[\mathbf{r}, \mathbf{p}, t'; z_{00}] = \frac{a - b^* z_{00}^*}{\sqrt{1 + |z_{00}|^2}}. \quad (\text{C10})$$

Here we took $z_f \rightarrow \infty$ for spin up and $z_f \rightarrow 0$ for spin down. We proceed by writing in more compact notation: we collect t', \mathbf{r} , and \mathbf{p} into x and set $\mathcal{M}_{0,I}[x] = d[x] e^{iS_{0,I}[x]}$. Now the spin-averaged probability is

$$\mathcal{P}_{\uparrow}(\mathbf{p}_f, z_{00}) = \frac{2}{\pi} \int_{\mathbb{C}} d^2 z_{00} \frac{1}{(1+|z_{00}|^2)^2} \left| \int \mathcal{D}x \frac{b[x] + a[x]z_{00}}{\sqrt{1+|z_{00}|^2}} \mathcal{M}_{0,I}[x] \right|^2 \quad (\text{C11})$$

$$= \frac{2}{\pi} \int \mathcal{D}x \int \mathcal{D}x' \mathcal{M}_{0,I}[x] \mathcal{M}_{0,I}^*[x'] \int_{\mathbb{C}} d^2 z_{00} \frac{1}{(1+|z_{00}|^2)^2} \left(\frac{b[x] + a[x]z_{00}}{\sqrt{1+|z_{00}|^2}} \right) \left(\frac{b^*[x'] + a^*[x']z_{00}^*}{\sqrt{1+|z_{00}|^2}} \right) \quad (\text{C12})$$

$$= \frac{2}{\pi} \int \mathcal{D}x \int \mathcal{D}x' \mathcal{M}_{0,I}[x] \mathcal{M}_{0,I}^*[x'] \underbrace{\int_{\mathbb{C}} d^2z_{00} \frac{(b[x] + a[x]z_{00})(b^*[x'] + a^*[x']z_{00}^*)}{(1 + |z_{00}|^2)^3}}_I. \quad (\text{C13})$$

Here we pull out the integral over spin states and do this separately:

$$I = \int_{\mathbb{C}} d^2z_{00} \frac{(b[x] + a[x]z_{00})(b^*[x'] + a^*[x']z_{00}^*)}{(1 + |z_{00}|^2)^3} \quad (\text{C14})$$

$$= \int_{\mathbb{C}} d^2z_{00} \frac{b[x]b^*[x'] + b[x]a^*[x']z_{00}^* + a[x]b^*[x']z_{00} + a[x]a^*[x']|z_{00}|^2}{(1 + |z_{00}|^2)^3} \quad (\text{C15})$$

$$= -2 \int_0^\infty du_0 \int_0^{2\pi} d\phi_0 \frac{b[x]b^*[x'] + b[x]a^*[x']u_0 e^{-i\phi_0} + a[x]b^*[x']u_0 e^{i\phi_0} + a[x]a^*[x']u_0^2}{(1 + u_0^2)^3} \quad (\text{C16})$$

$$= - \int_0^\infty u_0 du_0 \frac{4\pi (b[x]b^*[x'] + a[x]a^*[x']u_0^2)}{(1 + u_0^2)^3} \quad (\text{C17})$$

$$= \pi (b[x]b^*[x'] + a[x]a^*[x']). \quad (\text{C18})$$

Inserting the integral back into Eq. (C13) gives

$$\mathcal{P}_{\uparrow;(\mathbf{p}_f)} = \int \mathcal{D}x \int \mathcal{D}x' \mathcal{M}_{0,I}[x] \mathcal{M}_{0,I}^*[x'] \times [x'](b[x]b^*[x'] + a[x]a^*[x']) \quad (\text{C19})$$

$$= \left| \int \mathcal{D}x a[x] \mathcal{M}_{0,I}[x] \right|^2 + \left| \int \mathcal{D}x b[x] \mathcal{M}_{0,I}[x] \right|^2 = \mathcal{P}_{\uparrow;\uparrow}(\mathbf{p}_f) + \mathcal{P}_{\uparrow;\downarrow}(\mathbf{p}_f). \quad (\text{C20})$$

Given that, $\mathcal{M}_{\text{SO}}^\uparrow[\mathbf{r}, \mathbf{p}, t'; z_{00}] \rightarrow a$ as $z_{00} \rightarrow \infty$ and $\mathcal{M}_{\text{SO}}^\uparrow[\mathbf{r}, \mathbf{p}, t'; z_{00}] \rightarrow b$ as $z_{00} \rightarrow 0$. By the same logic $\mathcal{P}_{\downarrow;(\mathbf{p}_f)} = \mathcal{P}_{\downarrow;\uparrow}(\mathbf{p}_f) + \mathcal{P}_{\downarrow;\downarrow}(\mathbf{p}_f)$.

APPENDIX D: CHARACTERIZING THE DYNAMICAL SPIN COEFFICIENTS $a(t)$ AND $b(t)$

Given that we restrict dynamics to the zy plane and the orbital angular momentum consequently is in the x direction, the ODE for $a(t)$ and $b(t)$ [Eq. (37)] may be written as

$$\begin{aligned} \dot{a}(t) &= -\frac{i}{2c^2 r} \frac{dV}{dr} L_x(t) b^*(t), \\ \dot{b}(t) &= -\frac{i}{2c^2 r} \frac{dV}{dr} L_x(t) a^*(t). \end{aligned} \quad (\text{D1})$$

By writing $a(t)$ and $b(t)$ explicitly in terms of real and imaginary parts, this set of ODEs may be written as a 4-vector equation $\dot{\mathbf{x}}(t) = H_{\text{SO}}(t) \underline{\eta} \mathbf{x}(t)$ with $\mathbf{x}(t) = (\text{Re}[a(t)], \text{Im}[a(t)], \text{Re}[b(t)], \text{Im}[b(t)])$ and

$$\underline{\eta} = \begin{pmatrix} 0 & 0 & 0 & 1 \\ 0 & 0 & -1 & 0 \\ 0 & 1 & 0 & 0 \\ -1 & 0 & 0 & 0 \end{pmatrix}, \quad (\text{D2})$$

$$H_{\text{SO}}(t) = \frac{1}{2cr^2} \frac{dV}{dr} L_x(t) \quad (\text{D3})$$

Thus, $a(t)$ and $b(t)$ may be solved (see [114]) as

$$\begin{aligned} a(t) &= \mathbf{x}_a \cdot \left[\exp \left(\int dt H_{\text{SO}}(t) \underline{\eta} \right) \mathbf{x}_0 \right], \\ b(t) &= \mathbf{x}_b \cdot \left[\exp \left(\int dt H_{\text{SO}}(t) \underline{\eta} \right) \mathbf{x}_0 \right], \end{aligned} \quad (\text{D4})$$

where the dot product with $\mathbf{x}_a(t) = (1, i, 0, 0)$ selects the real and imaginary components of $a(t)$ and $\mathbf{x}_b = (0, 0, 1, i)$ selects the real and imaginary components of $b(t)$. The initial conditions are $a(0) = 1$ and $b(0) = 0$, which means $\mathbf{x}_0 = (1, 0, 0, 0)$, and this leads to the solutions

$$a(t) = \cos[S_{\text{SO}}(t)], \quad b(t) = -i \sin[S_{\text{SO}}(t)], \quad (\text{D5})$$

which are the solutions used in the discussion in Sec. VB.

APPENDIX E: RELATIVISTIC FORCE CORRECTIONS

Here we consider the equations of motion with relativistic correction to the kinetic energy to better understand why the core gets less strongly probed with than without these corrections. Hamilton's equations of motion are given by

$$\dot{\mathbf{r}} = \nabla_{\mathbf{p}} K[\mathbf{p}], \quad \dot{\mathbf{p}} = -\nabla_{\mathbf{r}} U[\mathbf{r}]. \quad (\text{E1})$$

Considering only the relativistic corrections to kinetic energy we have $K[\mathbf{p}] = \frac{1}{2} \mathbf{p}^2 - \frac{1}{8c^2} \mathbf{p}^4$, with $\nabla_{\mathbf{p}} K[\mathbf{p}] = (1 - \frac{1}{2c^2} \mathbf{p}^2) \mathbf{p}$. Taking the derivative of $\dot{\mathbf{r}}$ with respect to time and writing $\mathbf{F} = -\nabla_{\mathbf{r}} U$, we obtain a Newtonian-style force equation

$$\ddot{\mathbf{r}} = \left(1 - \frac{1}{2c^2} \underline{M} \right) \mathbf{F}, \quad (\text{E2})$$

where \underline{M} is a matrix given by $\underline{M} = \mathbb{1}_3 \mathbf{p}^2 + 2\mathbf{p} \otimes \mathbf{p}$. Thus, the matrix \underline{M} determines by how much the force is effectively reduced from the classical case. For example, in the case the electron is heading directly to the residual ion, $\mathbf{p} = (0, 0, v)$

and $\mathbf{F} = (0, 0, F)$,

$$\underline{\underline{M}} = \begin{pmatrix} v^2 & 0 & 0 \\ 0 & v^2 & 0 \\ 0 & 0 & 3v^2 \end{pmatrix} \quad (\text{E3})$$

leading to the equation

$$\ddot{z} = \left(1 - \frac{3v^2}{2c^2}\right)F. \quad (\text{E4})$$

While, in the case that the electron is traveling perpendicular to force due to the residual ion, $\mathbf{p} = (0, v, 0)$ and $\mathbf{F} = (0, 0, F)$, $\underline{\underline{M}}$ is the same as before, but a different component is nonzero, leading to the equation

$$\ddot{z} = \left(1 - \frac{v^2}{2c^2}\right)F. \quad (\text{E5})$$

This effective reduction of the central force will lead to the orbital radius increasing, and thus the core is probed less strongly. These aspects are discussed in Sec. VI of the main text.

-
- [1] G. E. Uhlenbeck and S. Goudsmit, Ersetzung der Hypothese vom unmechanischen Zwang durch eine Forderung bezüglich des inneren Verhaltens jedes einzelnen Elektrons, *Naturwissenschaften* **13**, 953 (1925).
- [2] P. Zeeman, The effect of magnetisation on the nature of light emitted by a substance, *Nature (London)* **55**, 347 (1897).
- [3] N. F. Mott, Scattering of electrons by gold, *Nature (London)* **124**, 986 (1929).
- [4] I. Barth and O. Smirnova, Spin-polarized electrons produced by strong-field ionization, *Phys. Rev. A* **88**, 013401 (2013).
- [5] A. Hartung, F. Morales, M. Kunitski, K. Henrichs, A. Laucke, M. Richter, T. Jahnke, A. Kalinin, M. Schöffler, L. P. H. Schmidt, M. Ivanov, O. Smirnova, and R. Dörner, Electron spin polarization in strong-field ionization of xenon atoms, *Nat. Photon.* **10**, 526 (2016).
- [6] P. B. Corkum, Plasma perspective on strong field multiphoton ionization, *Phys. Rev. Lett.* **71**, 1994 (1993).
- [7] F. Krausz and M. Ivanov, Attosecond physics, *Rev. Mod. Phys.* **81**, 163 (2009).
- [8] P. Salières, A. L’Huillier, P. Antoine, and M. Lewenstein, Study of The Spatial and Temporal Coherence of High-Order Harmonics, in *Advances In Atomic, Molecular, and Optical Physics*, Vol. 41, edited by B. Bederson and H. Walther (Academic, New York, 1999), pp. 83–142.
- [9] M. Lewenstein and A. L’Huillier, Principles of Single Atom Physics: High-Order Harmonic Generation, Above-Threshold Ionization and Non-Sequential Ionization, in *Strong Field Laser Physics*, Springer Series in Optical Sciences, edited by T. Brabec (Springer, New York, 2009), pp. 147–183.
- [10] M. F. Ciappina, J. A. Pérez-Hernández, A. S. Landsman, W. A. Okell, S. Zherebtsov, B. Förg, J. Schötz, L. Seiffert, T. Fennel, T. Shaaran, T. Zimmermann, A. Chacón, R. Guichard, A. Zaïr, J. W. G. Tisch, J. P. Marangos, T. Witting, A. Braun, S. A. Maier, L. Roso *et al.*, Attosecond physics at the nanoscale, *Rep. Prog. Phys.* **80**, 054401 (2017).
- [11] P. M. Paul, E. S. Toma, P. Breger, G. Mullot, F. Augé, Ph. Balcou, H. G. Muller, and P. Agostini, Observation of a train of attosecond pulses from high harmonic generation, *Science* **292**, 1689 (2001).
- [12] M. Hentschel, R. Kienberger, C. Spielmann, G. A. Reider, N. Milosevic, T. Brabec, P. Corkum, U. Heinzmann, M. Drescher, and F. Krausz, Attosecond metrology, *Nature (London)* **414**, 509 (2001).
- [13] M. Lewenstein, Ph. Balcou, M. Yu. Ivanov, A. L’Huillier, and P. B. Corkum, Theory of high-harmonic generation by low-frequency laser fields, *Phys. Rev. A* **49**, 2117 (1994).
- [14] P. Agostini, F. Fabre, G. Mainfray, G. Petite, and N. K. Rahman, Free-free transitions following six-photon ionization of Xenon atoms, *Phys. Rev. Lett.* **42**, 1127 (1979).
- [15] G. G. Paulus, W. Becker, W. Nicklich, and H. Walther, Rescattering effects in above-threshold ionization : A classical model, *J. Phys. B: At., Mol. Opt. Phys.* **27**, L703 (1994).
- [16] M. Lewenstein, K. C. Kulander, K. J. Schafer, and P. H. Bucksbaum, Rings in above-threshold ionization: A quasiclassical analysis, *Phys. Rev. A* **51**, 1495 (1995).
- [17] T. Zuo, A. D. Bandrauk, and P. B. Corkum, Laser-induced electron diffraction: A new tool for probing ultrafast molecular dynamics, *Chem. Phys. Lett.* **259**, 313 (1996).
- [18] H. Niikura, F. Légaré, R. Hasbani, A. D. Bandrauk, M. Y. Ivanov, D. M. Villeneuve, and P. B. Corkum, Sub-laser-cycle electron pulses for probing molecular dynamics, *Nature (London)* **417**, 917 (2002).
- [19] K. Amini and J. Biegert, Ultrafast electron diffraction imaging of gas-phase molecules, in *Advances In Atomic, Molecular, and Optical Physics*, Vol. 69, edited by L. F. Dimauuro, H. Perrin, and S. F. Yelin (Academic, New York, 2020), Chap. 3, pp. 163–231.
- [20] A. Sanchez, K. Amini, S.-J. Wang, T. Steinle, B. Belsa, J. Danek, A. T. Le, X. Liu, R. Moshhammer, T. Pfeifer, M. Richter, J. Ullrich, S. Gräfe, C. D. Lin, and J. Biegert, Molecular structure retrieval directly from laboratory-frame photoelectron spectra in laser-induced electron diffraction, *Nat. Commun.* **12**, 1520 (2021).
- [21] U. D. Giovannini, J. Küpper, and A. Trabattoni, New perspectives in time-resolved laser-induced electron diffraction, *J. Phys. B: At., Mol. Opt. Phys.* **56**, 054002 (2023).
- [22] Y. Huismans, A. Rouzée, A. Gijbetsen, J. H. Jungmann, A. S. Smolkowska, P. S. W. M. Logman, F. Lépine, C. Cauchy, S. Zamith, T. Marchenko, J. M. Bakker, G. Berden, B. Redlich, A. F. G. van der Meer, H. G. Muller, W. Vermin, K. J. Schafer, M. Spanner, M. Yu. Ivanov, O. Smirnova *et al.*, Time-resolved Holography with photoelectrons, *Science* **331**, 61 (2011).
- [23] D. D. Hickstein, P. Ranitovic, S. Witte, X. M. Tong, Y. Huismans, P. Arpin, X. Zhou, K. E. Keister, C. W. Hogle, B. Zhang, C. Ding, P. Johnsson, N. Toshima, M. J. J. Vrakking, M. M. Murnane, and H. C. Kapteyn, Direct visualization of laser-driven electron multiple scattering and tunneling distance in strong-field ionization, *Phys. Rev. Lett.* **109**, 073004 (2012).
- [24] C. F. d. M. Faria and A. S. Maxwell, It is all about phases: Ultrafast holographic photoelectron imaging, *Rep. Prog. Phys.* **83**, 034401 (2020).

- [25] H. R. Reiss, Complete Keldysh theory and its limiting cases, *Phys. Rev. A* **42**, 1476 (1990).
- [26] H. R. Reiss, Relativistic strong-field photoionization, *J. Opt. Soc. Am. B* **7**, 574 (1990).
- [27] M. Protopapas, C. H. Keitel, and P. L. Knight, Atomic physics with super-high intensity lasers, *Rep. Prog. Phys.* **60**, 389 (1997).
- [28] M. W. Walser, D. J. Urbach, K. Z. Hatsagortsyan, S. X. Hu, and C. H. Keitel, Spin and radiation in intense laser fields, *Phys. Rev. A* **65**, 043410 (2002).
- [29] M. Klaiber, E. Yakoboylu, and K. Z. Hatsagortsyan, Above-threshold ionization with highly charged ions in superstrong laser fields. I. Coulomb-corrected strong-field approximation, *Phys. Rev. A* **87**, 023417 (2013).
- [30] M. Klaiber, E. Yakoboylu, and K. Z. Hatsagortsyan, Above-threshold ionization with highly charged ions in superstrong laser fields. II. Relativistic Coulomb-corrected strong-field approximation, *Phys. Rev. A* **87**, 023418 (2013).
- [31] M. Klaiber, E. Yakoboylu, C. Müller, H. Bauke, G. G. Paulus, and K. Z. Hatsagortsyan, Spin dynamics in relativistic ionization with highly charged ions in super-strong laser fields, *J. Phys. B: At., Mol. Opt. Phys.* **47**, 065603 (2014).
- [32] M. Klaiber, K. Z. Hatsagortsyan, J. Wu, S. S. Luo, P. Grugan, and B. C. Walker, Limits of strong field rescattering in the relativistic regime, *Phys. Rev. Lett.* **118**, 093001 (2017).
- [33] M. Klaiber, J. Daněk, E. Yakoboylu, K. Z. Hatsagortsyan, and C. H. Keitel, Strong-field ionization via a high-order Coulomb-corrected strong-field approximation, *Phys. Rev. A* **95**, 023403 (2017).
- [34] M. Klaiber, K. Z. Hatsagortsyan, and C. H. Keitel, Relativistic analytical R -matrix theory for strong-field ionization, *Phys. Rev. A* **107**, 023107 (2023).
- [35] L. V. Keldysh, Ionization in the field of a strong electromagnetic wave, *J. Exptl. Theoret. Phys. (U.S.S.R.)* **47**, 1945 (1964) [*Sov. Phys.–JETP* **20**, 1307 (1965)].
- [36] F. H. Faisal, Multiple absorption of laser photons by atoms, *J. Phys. B: At. Mol. Phys.* **6**, L89 (1973).
- [37] H. R. Reiss, Effect of an intense electromagnetic field on a weakly bound system, *Phys. Rev. A* **22**, 1786 (1980).
- [38] R. Santra, R. W. Dunford, and L. Young, Spin-orbit effect on strong-field ionization of krypton, *Phys. Rev. A* **74**, 043403 (2006).
- [39] U. Fano, Spin orientation of photoelectrons ejected by circularly polarized light, *Phys. Rev.* **178**, 131 (1969).
- [40] P. Lambropoulos, Spin-orbit coupling and photoelectron polarization in multiphoton ionization of atoms, *Phys. Rev. Lett.* **30**, 413 (1973).
- [41] J. Kaushal and O. Smirnova, Looking inside the tunnelling barrier III: Spin polarisation in strong field ionisation from orbitals with high angular momentum, *J. Phys. B: At., Mol. Opt. Phys.* **51**, 174003 (2018).
- [42] I. Barth and O. Smirnova, Nonadiabatic tunneling in circularly polarized laser fields: Physical picture and calculations, *Phys. Rev. A* **84**, 063415 (2011).
- [43] T. Herath, L. Yan, S. K. Lee, and W. Li, Strong-field ionization rate depends on the sign of the magnetic quantum number, *Phys. Rev. Lett.* **109**, 043004 (2012).
- [44] S. Eckart, M. Kunitski, M. Richter, A. Hartung, J. Rist, F. Trinter, K. Fehre, N. Schlott, K. Henrichs, L. P. H. Schmidt, T. Jahnke, M. Schöffler, K. Liu, I. Barth, J. Kaushal, F. Morales, M. Ivanov, O. Smirnova, and R. Dörner, Ultrafast preparation and detection of ring currents in single atoms, *Nat. Phys.* **14**, 701 (2018).
- [45] D. Trabert, A. Hartung, S. Eckart, F. Trinter, A. Kalinin, M. Schöffler, L. P. H. Schmidt, T. Jahnke, M. Kunitski, and R. Dörner, Spin and angular momentum in strong-field Ionization, *Phys. Rev. Lett.* **120**, 043202 (2018).
- [46] Y. Hu, K. Liu, K. Renziehausen, Y. Tian, Q. Zhang, M. Li, Y. Zhou, and P. Lu, Effect of spin-orbit coupling in laser-induced ionization of atoms, *Phys. Rev. A* **108**, 023113 (2023).
- [47] I. A. Ivanov, Relativistic calculation of the electron-momentum shift in tunneling ionization, *Phys. Rev. A* **91**, 043410 (2015).
- [48] N. Haram, I. Ivanov, H. Xu, K. T. Kim, A. Atia-tul-Noor, U. S. Sainadh, R. D. Glover, D. Chetty, I. V. Litvinyuk, and R. T. Sang, Relativistic nondipole effects in strong-field atomic ionization at moderate Intensities, *Phys. Rev. Lett.* **123**, 093201 (2019).
- [49] D. Zille, D. Seipt, M. Möller, S. Fritzsche, S. Gräfe, C. Müller, and G. G. Paulus, Spin-dependent rescattering in strong-field ionization of helium, *J. Phys. B: At., Mol. Opt. Phys.* **50**, 065001 (2017).
- [50] D. B. Milošević, Spin-dependent effects in high-order above-threshold ionization: Spin-orbit interaction and exchange effects, *J. Phys. B: At., Mol. Opt. Phys.* **50**, 164003 (2017).
- [51] N. Rohringer and R. Santra, Multichannel coherence in strong-field ionization, *Phys. Rev. A* **79**, 053402 (2009).
- [52] I. Barth and O. Smirnova, Hole dynamics and spin currents after ionization in strong circularly polarized laser fields, *J. Phys. B: At., Mol. Opt. Phys.* **47**, 204020 (2014).
- [53] J. Kaushal, F. Morales, L. Torlina, M. Ivanov, and O. Smirnova, Spin-orbit Larmor clock for ionization times in one-photon and strong-field regimes, *J. Phys. B: At., Mol. Opt. Phys.* **48**, 234002 (2015).
- [54] M. Kübel, Z. Dube, A. Y. Naumov, D. M. Villeneuve, P. B. Corkum, and A. Staudte, Spatiotemporal imaging of valence electron motion, *Nat. Commun.* **10**, 1042 (2019).
- [55] S. Carlström, J. M. Dahlström, M. Y. Ivanov, and S. Patchkovskii, Rydberg atomic antenna in strongly driven multielectron atoms, *Phys. Rev. A* **106**, 043114 (2022).
- [56] G. A. Stewart, P. Hoerner, D. A. Debrah, S. K. Lee, H. B. Schlegel, and W. Li, Attosecond imaging of electronic wave packets, *Phys. Rev. Lett.* **130**, 083202 (2023).
- [57] S. Zhong, J. Vinbladh, D. Busto, R. J. Squibb, M. Isinger, L. Neoričić, H. Laurell, R. Weissenbilder, C. L. Arnold, R. Feifel, J. M. Dahlström, G. Wendin, M. Gisselbrecht, E. Lindroth, and A. L'Huillier, Attosecond electron-spin dynamics in Xe 4d photoionization, *Nat. Commun.* **11**, 5042 (2020).
- [58] S. Carlström, J. M. Dahlström, M. Y. Ivanov, O. Smirnova, and S. Patchkovskii, Control of spin polarization through recollisions, *Phys. Rev. A* **108**, 043104 (2023).
- [59] X. Y. Lai, C. Poli, H. Schomerus, and C. F. d. M. Faria, Influence of the Coulomb potential on above-threshold ionization: A quantum-orbit analysis beyond the strong-field approximation, *Phys. Rev. A* **92**, 043407 (2015).
- [60] X. Lai, S. Yu, Y. Huang, L. Hua, C. Gong, W. Quan, C. F. d. M. Faria, and X. Liu, Near-threshold photoelectron holography beyond the strong-field approximation, *Phys. Rev. A* **96**, 013414 (2017).

- [61] A. S. Maxwell, A. Al-Jawahiry, T. Das, and C. F. d. M. Faria, Coulomb-corrected quantum interference in above-threshold ionization: Working towards multi-trajectory electron holography, *Phys. Rev. A* **96**, 023420 (2017).
- [62] A. S. Maxwell, A. Al-Jawahiry, X. Y. Lai, and C. F. d. M. Faria, Analytic quantum-interference conditions in Coulomb corrected photoelectron holography, *J. Phys. B: At., Mol. Opt. Phys.* **51**, 044004 (2018).
- [63] A. S. Maxwell and C. F. d. M. Faria, Coulomb-free and Coulomb-distorted recolliding quantum orbits in photoelectron holography, *J. Phys. B: At., Mol. Opt. Phys.* **51**, 124001 (2018).
- [64] A. S. Maxwell, S. V. Popruzhenko, and C. F. d. M. Faria, Treating branch cuts in quantum trajectory models for photoelectron holography, *Phys. Rev. A* **98**, 063423 (2018).
- [65] W. Becker, F. Grasbon, R. Kopold, D. B. Milošević, G. G. Paulus, and H. Walther, Above-Threshold Ionization: From Classical Features to Quantum Effects, in *Advances In Atomic, Molecular, and Optical Physics*, Vol. 48, edited by B. Bederson and H. Walther (Academic, New York, 2002), pp. 35–98.
- [66] D. B. Milošević, G. G. Paulus, D. Bauer, and W. Becker, Above-threshold ionization by few-cycle pulses, *J. Phys. B: At., Mol. Opt. Phys.* **39**, R203 (2006).
- [67] K. Amini, J. Biegert, F. Calegari, A. Chacón, M. F. Ciappina, A. Dauphin, D. K. Efimov, C. F. d. M. Faria, K. Giergiel, P. Gniewek, A. S. Landsman, M. Lesiuk, M. Mandrysz, A. S. Maxwell, R. Moszyński, L. Ortmann, J. A. Pérez-Hernández, A. Picón, E. Pisanty, J. Prauzner-Bechcicki *et al.*, Symphony on strong field approximation, *Rep. Prog. Phys.* **82**, 116001 (2019).
- [68] H. P. Kang, A. S. Maxwell, D. Trabert, X. Y. Lai, S. Eckart, M. Kunitski, M. Schöffler, T. Jahnke, X. B. Bian, R. Dörner, and C. F. d. M. Faria, Holographic detection of parity in atomic and molecular orbitals, *Phys. Rev. A* **102**, 013109 (2020).
- [69] A. S. Maxwell, C. Figueira De Morisson Faria, X. Y. Lai, R. P. Sun, and X. J. Liu, Spiral-like holographic structures: Unwinding interference carpets of Coulomb-distorted orbits in strong-field ionization, *Phys. Rev. A* **102**, 033111 (2020).
- [70] N. Werby, A. S. Maxwell, R. Forbes, P. H. Bucksbaum, and C. F. d. M. Faria, Dissecting subcycle interference in photoelectron holography, *Phys. Rev. A* **104**, 013109 (2021).
- [71] N. Werby, A. S. Maxwell, R. Forbes, C. F. d. M. Faria, and P. H. Bucksbaum, Probing two-path electron quantum interference in strong-field ionization with time-correlation filtering, *Phys. Rev. A* **106**, 033118 (2022).
- [72] S. Brennecke, N. Eicke, and M. Lein, Gouy's phase anomaly in electron waves produced by strong-field ionization, *Phys. Rev. Lett.* **124**, 153202 (2020).
- [73] L. C. Rodriguez, T. Rook, B. B. Augstein, A. S. Maxwell, and C. F. d. M. Faria, Forward and hybrid path-integral methods in photoelectron holography: Sub-barrier corrections, initial sampling and momentum mapping, *Phys. Rev. A* **108**, 033114 (2023).
- [74] M. B. Carlsen, E. Hansen, L. B. Madsen, and A. S. Maxwell, Advanced momentum sampling and Maslov phases for a precise semiclassical model of strong-field ionization, *New J. Phys.* **26**, 023025 (2024).
- [75] H. Kleinert, *Path Integrals in Quantum Mechanics, Statistics, Polymer Physics, and Financial Markets*, 5th ed. (World Scientific, Singapore, 2009).
- [76] N. I. Shvetsov-Shilovski, Semiclassical two-step model for ionization by a strong laser pulse: Further developments and applications, *Eur. Phys. J. D* **75**, 130 (2021).
- [77] T.-M. Yan, S. V. Popruzhenko, M. J. J. Vrakking, and D. Bauer, Low-energy structures in strong field ionization revealed by quantum orbits, *Phys. Rev. Lett.* **105**, 253002 (2010).
- [78] V. Tulsy and D. Bauer, QPROP with faster calculation of photoelectron spectra, *Comput. Phys. Commun.* **251**, 107098 (2020).
- [79] C. F. d. M. Faria, H. Schomerus, and W. Becker, High-order above-threshold ionization: The uniform approximation and the effect of the binding potential, *Phys. Rev. A* **66**, 043413 (2002).
- [80] L. Kocia and A. Klaes, Semiclassical treatment of quantum propagation with nonlinear classical dynamics: A third-order thawed Gaussian approximation, *Phys. Rev. E* **94**, 032211 (2016).
- [81] P. Strange, *Relativistic Quantum Mechanics: With Applications in Condensed Matter and Atomic Physics*, 1st ed. (Cambridge University Press, Cambridge, 1998).
- [82] H. R. Reiss, Limits on tunneling theories of strong-field ionization, *Phys. Rev. Lett.* **101**, 043002 (2008).
- [83] J. R. Klauder, Path integrals and stationary-phase approximations, *Phys. Rev. D* **19**, 2349 (1979).
- [84] M. Pletyukhov, Ch. Amann, M. Mehta, and M. Brack, Semiclassical theory of spin-orbit interactions using spin coherent states, *Phys. Rev. Lett.* **89**, 116601 (2002).
- [85] B. H. Bransden and C. J. Joachain, *Physics of Atoms and Molecules* (Longman Scientific & Technical, Burnt Mill, Harlow, 1983).
- [86] E. A. Kochetov, SU(2) coherent-state path integral, *J. Math. Phys.* **36**, 4667 (1995).
- [87] M. Pletyukhov and O. Zaitsev, Semiclassical theory of spin orbit interaction in the extended phase space, *J. Phys. A: Math. Gen.* **36**, 5181 (2003).
- [88] K. Morten, A path integral approach to the spin-orbit interaction, Ph.D. thesis, Nano-Science Center, Copenhagen University, 2008.
- [89] T. J. Lemmon and A. R. Mondragon, Kepler's orbits and special relativity in introductory classical mechanics, [arxiv:1012.5438](https://arxiv.org/abs/1012.5438).
- [90] C. I. Blaga, J. Xu, A. D. DiChiara, E. Sistrunk, K. Zhang, P. Agostini, T. A. Miller, L. F. DiMauro, and C. D. Lin, Imaging ultrafast molecular dynamics with laser-induced electron diffraction, *Nature (London)* **483**, 194 (2012).
- [91] B. Wolter, M. G. Pullen, A.-T. Le, M. Baudisch, K. Doblhoff-Dier, A. Senftleben, M. Hemmer, C. D. Schröter, J. Ullrich, T. Pfeifer, R. Moshhammer, S. Gräfe, O. Vendrell, C. D. Lin, and J. Biegert, Ultrafast electron diffraction imaging of bond breaking in di-ionized acetylene, *Science* **354**, 308 (2016).
- [92] A. Gorlach, O. Neufeld, N. Rivera, O. Cohen, and I. Kaminer, The quantum-optical nature of high harmonic generation, *Nat. Commun.* **11**, 4598 (2020).
- [93] M. Lewenstein, M. F. Ciappina, E. Pisanty, J. Rivera-Dean, P. Stammer, T. Lamprou, and P. Tzallas, Generation of optical Schrödinger cat states in intense laser-matter interactions, *Nat. Phys.* **17**, 1104 (2021).
- [94] P. Stammer, J. Rivera-Dean, T. Lamprou, E. Pisanty, M. F. Ciappina, P. Tzallas, and M. Lewenstein, High photon number

- entangled states and coherent state superposition from the extreme ultraviolet to the far infrared, *Phys. Rev. Lett.* **128**, 123603 (2022).
- [95] J. Rivera-Dean, P. Stammer, A. S. Maxwell, Th. Lamprou, P. Tzallas, M. Lewenstein, and M. F. Ciappina, Light-matter entanglement after above-threshold ionization processes in atoms, *Phys. Rev. A* **106**, 063705 (2022).
- [96] P. Stammer, J. Rivera-Dean, A. Maxwell, T. Lamprou, A. Ordóñez, M. F. Ciappina, P. Tzallas, and M. Lewenstein, Quantum electrodynamics of intense laser-matter interactions: A tool for quantum state engineering, *PRX Quantum* **4**, 010201 (2023).
- [97] A. Pizzi, A. Gorlach, N. Rivera, A. Nunnenkamp, and I. Kaminer, Light emission from strongly driven many-body systems, *Nat. Phys.* **19**, 551 (2023).
- [98] M. Even Tzur, M. Birk, A. Gorlach, M. Krüger, I. Kaminer, and O. Cohen, Photon-statistics force in ultrafast electron dynamics, *Nat. Photon.* **17**, 501 (2023).
- [99] A. S. Maxwell, G. S. J. Armstrong, M. Ciappina, E. Pisanty, Y. Kang, A. Brown, M. Lewenstein, and C. F. d. M. Faria, Manipulating twisted electrons in strong field ionization, *Faraday Discuss.* **228**, 394 (2021).
- [100] Y. Kang, E. Pisanty, M. Ciappina, M. Lewenstein, C. F. d. M. Faria, and A. S. Maxwell, Conservation laws for electron vortices in strong-field ionisation, *Eur. Phys. J. D* **75**, 199 (2021).
- [101] X. B. Planas, A. Ordóñez, M. Lewenstein, and A. S. Maxwell, Ultrafast imaging of molecular chirality with photoelectron vortices, *Phys. Rev. Lett.* **129**, 233201 (2022).
- [102] A. S. Maxwell, L. B. Madsen, and M. Lewenstein, Entanglement of orbital angular momentum in non-sequential double ionization, *Nat. Commun.* **13**, 4706 (2022).
- [103] S. V. B. Jensen, M. M. Lund, and L. B. Madsen, Nondipole strong-field-approximation Hamiltonian, *Phys. Rev. A* **101**, 043408 (2020).
- [104] L. B. Madsen, Nondipole effects in tunneling ionization by intense laser pulses, *Phys. Rev. A* **105**, 043107 (2022).
- [105] S. Brennecke and M. Lein, High-order above-threshold ionization beyond the electric dipole approximation: Dependence on the atomic and molecular structure, *Phys. Rev. A* **98**, 063414 (2018).
- [106] L. B. Madsen, Disappearance and reappearance of above-threshold-ionization peaks, *Phys. Rev. A* **106**, 043118 (2022).
- [107] C. T. L. Smeenk, L. Arissian, B. Zhou, A. Mysyrowicz, D. M. Villeneuve, A. Staudte, and P. B. Corkum, Partitioning of the linear photon momentum in multiphoton ionization, *Phys. Rev. Lett.* **106**, 193002 (2011).
- [108] H. R. Reiss, Relativistic effects in nonrelativistic ionization, *Phys. Rev. A* **87**, 033421 (2013).
- [109] N. Haram, R. T. Sang, and I. V. Litvinyuk, Transverse electron momentum distributions in strong-field ionization: Nondipole and Coulomb focusing effects, *J. Phys. B: At., Mol. Opt. Phys.* **53**, 154005 (2020).
- [110] B. Wolter, M. G. Pullen, M. Baudisch, M. Sclafani, M. Hemmer, A. Senftleben, C. D. Schröter, J. Ullrich, R. Moshhammer, and J. Biegert, Strong-field physics with Mid-IR fields, *Phys. Rev. X* **5**, 021034 (2015).
- [111] N. I. Shvetsov-Shilovski, M. Lein, L. B. Madsen, E. Räsänen, C. Lemell, J. Burgdörfer, D. G. Arbó, and K. Tórkési, Semi-classical two-step model for strong-field ionization, *Phys. Rev. A* **94**, 013415 (2016).
- [112] A. M. Perelomov, V. S. Popov, and M. Terent'ev, Ionization of atoms in an alternating electrical field, *J. Exptl. Theoret. Phys. (U.S.S.R.)* **50**, 1393 (1966) [*Sov. Phys.–JETP* **23**, 924 (1966)].
- [113] C. Z. Bisgaard and L. B. Madsen, Tunneling ionization of atoms, *Am. J. Phys.* **72**, 249 (2004).
- [114] W. A. Adkins and M. G. Davidson, Linear systems of differential equations, in *Ordinary Differential Equations*, Undergraduate Texts in Mathematics, edited by W. A. Adkins and M. G. Davidson (Springer, New York, 2012), pp. 629–721.
- [115] M. M. Mizrahi, The Weyl correspondence and path integrals, *J. Math. Phys.* **16**, 2201 (1975).